Plasmodium falciparum quinine resistance is multifactorial and includes a role for the drug/metabolite transporters PfCRT and DMT1

Mariko Kanai[1,2], Sachel Mok[1,2,3], Tomas Yeo[1,2¶], Melanie J. Shears[4,5¶], Jin H. Jeon[1,2], Sunil K. Narwal[1,2], Leila S. Ross[1], Meseret T. Haile[1], Abhai K. Tripathi[4,5], Godfree Mlambo[4,5], Jonathan Kim[6], Eva Gil-Iturbe[7], John Okombo[1,2], Heekuk Park[3], Kharizta Wiradiputri[1,2], Kurt E. Ward[1,2], Felix D. Rozenberg[3], Kate J. Fairhurst[1,2], Talia S. Bloxham[2,3], Jessica L. Bridgford[1,2], Tanaya R. Sheth[1,2], Marcus C.S. Lee[8,9], Jennifer L. Small-Saunders[2,3], Filippo Mancia[6], Matthias Quick[6,7,10], Anne-Catrin Uhlemann[2,3], Photini Sinnis[4,5], David A. Fidock[1-3*]

[1]Department of Microbiology & Immunology, Columbia University Irving Medical Center, NY, USA; [2]Center for Malaria Therapeutics and Antimicrobial Resistance, Columbia University Irving Medical Center, NY, USA; [3]Division of Infectious Diseases, Department of Medicine, Columbia University Irving Medical Center, NY, USA; [4]Department of Molecular Microbiology and Immunology, Johns Hopkins Bloomberg School of Public Health, Baltimore, MD, USA; [5]Johns Hopkins Malaria Research Institute, Johns Hopkins University, Baltimore, MD, USA; [6]Department of Physiology and Cellular Biophysics, Columbia University Irving Medical Center, NY, USA; [7]Department of Psychiatry, Columbia University Irving Medical Center, NY, USA; [8]Wellcome Sanger Institute, Wellcome Genome Campus, Hinxton, UK; [9]Biological Chemistry and Drug Discovery, Wellcome Centre for Anti-Infectives Research, University of Dundee, Dundee, UK; [10]Area Neuroscience - Molecular Therapeutics, New York State Psychiatric Institute, NY, USA

¶These authors contributed equally to this work.

*Corresponding author's email address: df2260@cumc.columbia.edu

Abstract

The genetic basis of *Plasmodium falciparum* resistance to quinine (QN), a drug used to treat severe malaria, has long been enigmatic. To gain further insight, we used FRG-NOD human liver-chimeric mice to conduct a *P. falciparum* genetic cross between QN-resistant (Cam3.II) and QN-sensitive (NF54) parasites, which also differ in their susceptibility to chloroquine (CQ). By applying different selective conditions to progeny pools prior to cloning, we recovered 120 unique recombinant progeny. Drug profiling and quantitative trait loci analyses of the progeny revealed predominant peaks on chromosomes 7 and 12 associated with CQ and QN resistance, that is consistent with a multifactorial mechanism of resistance for these compounds. CQ and monodesethyl-CQ (md-CQ) resistance mapped to a chromosome 7 region harboring *pfcrt* as expected. However, for QN, resistance mapped to a dominant chromosome 7 peak centered 295 kb downstream of *pfcrt,* with *pfcrt* showing a smaller peak. We identified the drug/metabolite transporter 1 (DMT1) as the top chromosome 7 candidate due to its structural similarity to PfCRT and proximity to the peak. Deleting DMT1 in QN-resistant Cam3.II parasites significantly sensitized the parasite to QN but not to the other drugs tested, suggesting that DMT1 mediates QN response specifically. We localized DMT1 to structures associated with vesicular trafficking, as well as the parasitophorous vacuolar membrane, lipid bodies, and the digestive vacuole. We also observed that mutant DMT1 transports more QN than the wild-type isoform *in vitro*. Gene editing confirmed an additional role for mutant PfCRT in mediating QN resistance. In addition, we identified an ATP-dependent zinc metalloprotease (FtsH1) as one of the top candidates in the chromosome 12 locus and confirmed its role as a potential mediator of QN resistance and a modulator of md-CQ resistance using CRISPR/Cas9 SNP-edited lines. Interestingly, this chromosome 12 region mapped to resistance to both CQ and QN and was preferentially co-inherited with *pfcrt*. Our study demonstrates that DMT1 is a novel marker of QN resistance and that a new chromosome 12 locus associates with CQ and QN response, with *ftsh1* as a potential candidate, suggesting these genes in addition to *pfcrt* should be genotyped in surveillance and clinical settings.

Introduction

In 2023, there were an estimated 263 million cases of malaria, and an estimated 597,000 deaths, mostly African children[1]. Treatment of *Plasmodium falciparum* uncomplicated malaria depends on artemisinin-based combination therapies (ACTs), which combine fast-acting yet rapidly cleared artemisinin (ART) derivatives with longer-lasting partner drugs (mostly lumefantrine or amodiaquine). Artesunate is also the first-line treatment for severe, life-threatening malaria.

Alarmingly, *P. falciparum* parasites have now acquired partial resistance to ART derivatives in multiple African countries, having earlier saturated the greater Mekong Subregion in Southeast Asia[2,3]. Given the potential for widespread *P. falciparum* resistance to ARTs in Africa and the possible loss of ACT efficacy, alternative drugs with distinct modes of action are urgently needed. Trials are underway with several candidate drugs[4], however their rollout is years away. A potential alternative is to reintroduce licensed drugs such as QN, including for treating severe malaria. QN is also recommended (alone or with clindamycin) to treat *P. falciparum* malaria infections in pregnant women during the first trimester[1,5]. This drug has largely retained clinical efficacy since its first use in the 1600s, with resistance being slow to develop. QN resistance was first reported in ~1910 in Brazil, with subsequent reports from areas in South America, Africa, and Southeast Asia[6]. In these cases, QN resistance was usually low-grade, with QN having a delayed or reduced effect. QN treatment failure may result from parasite resistance[7] or other factors including variability in QN pharmacokinetics, compliance, and drug quality.

Here, we sought to gain a better understanding of genetic factors associated with QN resistance. This mechanism is thought to be multifactorial and has been partially associated with sequence changes in the *P. falciparum* chloroquine resistance transporter (*pfcrt)* (via single nucleotide polymorphisms (SNPs)), multidrug resistance protein 1 (*pfmdr1)* (both copy number and SNPs), sodium/hydrogen exchanger (*pfnhe-1)* (DNNND repeat polymorphisms), and the HECT E3 ubiquitin ligase *pfut* (SNPs)[8-13]. *pfnhe-1* and *pfut*, however, are minor strain-specific determinants at best, suggesting the

involvement of other genetic loci. QN, mefloquine (MFQ), and lumefantrine (LMF) are all classified as aryl-amino alcohols (**Extended Data 1a**) and appear to share partially overlapping modes of action, although the exact mechanisms remain unclear[14].

We also explored CQ, a 4-aminoquinoline (**Extended Data 1a**) and former first-line drug for *P. falciparum* that is still used to treat *P. vivax* malaria. CQ acts on the heme detoxification pathway by diffusing into the acidic digestive vacuole (DV), where it is protonated and binds to heme. This binding prevents heme detoxification into hemozoin (Hz), with free heme and heme-CQ adducts killing the parasite. PfCRT is the primary determinant of CQ resistance, with a minor contribution from mutant PfMDR1, which, like PfCRT, is a DV membrane transporter[10,15-19]. Both mutant *pfcrt* and *pfmdr1* are selected against in favor of their wild-type alleles in regions that use artemether-lumefantrine, the major ACT across Africa[20-22].

Genetic crosses are a powerful forward genetics tool to investigate the molecular basis of a variety of phenotypes including drug resistance. These studies have identified mutations in *dhps, dhfr* and *pfcrt* as primary determinants of resistance to sulfadoxine, pyrimethamine and CQ, respectively[23-26], and have been applied to study ART resistance mechanisms[27,28]. This methodology has been empowered by the development of a human liver-chimeric mouse model that obviates the earlier requirement for splenectomized monkeys[29]. Here, we applied this model to explore *P. falciparum* resistance to QN and CQ.

Results

Implementing a genetic cross to map markers of QN and CQ resistance

To identify markers of QN resistance, we implemented a genetic cross between Cam3.II and NF54 parasites (**Fig.1a**). Cam3.II is resistant to QN and CQ and originates from Southeast Asia[30,31]. This parasite expresses genetic variants of *pfcrt* and *pfut* that have been partially associated with QN resistance, as well as the *pfmdr1* N86/Y184F variant that does not associate with QN[10,13,18,32]. Cam3.II also harbors two copies of *pfmdr1* (**Fig. 1a**). NF54 is sensitive to both drugs and is wild-type at these three single-copy genes.

122 Mean QN and CQ IC_{50} values (in media with human serum) for Cam3.II were ~90 nM,
123 and for NF54 were ~10 nM. Based on our whole-genome sequence analysis, Cam3.II
124 and NF54 differ at 13,116 SNP positions, providing ample resolution to genetically map
125 primary and secondary mediators of resistance to both drugs.
126
127 To achieve this cross, we mixed mature NF54 and Cam3.II gametocytes at a 1:1 ratio
128 and fed them to female *Anopheles stephensi* mosquitoes[33] (**Extended Data 2a**). In the
129 midgut, gamete formation and subsequent sexual reproduction and recombination can
130 generate thousands of haploid sporozoites that migrate to the salivary glands, ready to
131 infect a mammalian host. Following parasitized blood feeds, we observed an infection
132 prevalence of ~85%, with ~20 oocysts resulting in ~40,000 salivary gland sporozoites per
133 mosquito (**Table S1**). We then infected four FRG NOD human liver-chimeric (huHep)
134 mice with ~60,000 to 200,000 progeny sporozoites per mouse. Parasites were inoculated
135 via mosquito bite or intravenously. After six days of liver-stage development, human red
136 blood cells (RBCs) were infused and on day seven, blood was drawn to capture haploid
137 asexual blood stage (ABS) parasites. These progeny were cultured *in vitro* for one to two
138 48 h generations of intra-erythrocytic development and replication before
139 cryopreservation.
140
141 **Combining bulk progeny cloning with differential drug selections yields 120 unique**
142 **recombinant progeny**
143 We thawed progeny bulk freezes from the four mice (A–D), expanded these cultures in
144 serum-containing media without drug pressure ('no drug bulks'), or under various CQ and
145 QN concentrations for 3–4 days, and cloned the progeny by limiting dilution (**Extended**
146 **Data 2b,c**). Recombinants were identified by SNP and microsatellite (MS) genotyping
147 and confirmed by whole-genome sequencing.
148
149 For each progeny, we classified alleles at each of the 13,116 SNP positions (**Table S2**)
150 that distinguish the parents. A subset of 1,836 SNPs was then used to generate genetic
151 maps, yielding a single linkage group for each of the 14 chromosomes. The recombination
152 rate of 13.7kb/cM was consistent with prior crosses[28,29,34-37] (**Table S3**). In total, the

153 progeny segregated into 120 unique recombinant haplotypes (**Table S4** and **Fig. 1b**). 55
154 were obtained without drug pressure prior to cloning. Of these, 45 (82%) were wild-type
155 for *pfcrt*, consistent with mutant *pfcrt* exerting a fitness cost in the absence of positive
156 selection. Pressuring with various concentrations of CQ or QN pressure yielded an
157 additional 65 haplotypes (**Fig. 1b**). Some QN selections included two to three rounds with
158 increasing concentrations, yielding four of the 65 unique haplotypes, suggesting that high-
159 grade selection can help to recover rare recombinants (and potentially those with a fitness
160 cost). Only 5 unique recombinant haplotypes were represented by progeny obtained in
161 both the CQ and QN selections, suggesting non-identical mechanisms of resistance to
162 these drugs.
163
164 Most recombinant progeny did not show any major allele frequency skews across their
165 genomes that deviated from the expected ~40–60% parental allele frequencies
166 (**Extended Data 3** and **Table S4**). As expected, all CQ-selected progeny possessed
167 mutant *pfcrt* from the Cam3.II parent (matching the well-characterized Dd2 allele;
168 **Supplemental Fig. 1a**). We obtained 26 haplotypes from progeny bulk pools selected
169 with QN at 95 nM (~1× QN IC_{50} for Cam3.II) or higher concentrations, of which 17 (65%)
170 had wild-type (WT) *pfcrt* and 15 (58%) had WT *dmt1* (**Supplemental Fig. 1b**). We noted
171 some enrichment for mutant *pfcrt* in parasites selected with QN (**Supplemental Fig. 1a**),
172 suggesting a role for this chromosomal region in QN resistance.
173
174 **Bulk segregant analysis identifies two quantitative trait loci peaks on chromosome**
175 **7 that associate with quinine resistance**
176 We then applied bulk segregant analysis (also known as linkage group selection analysis)
177 to determine genetic loci associated with QN resistance. This approach employed QN
178 pressure on bulk progeny pools, followed by whole-genome sequencing to measure allele
179 frequency changes and identify genetic loci associated with the trait of interest. By
180 pressuring four bulk cultures for 4 days with different concentrations of QN (~1.5, 2.0, or
181 2.6× IC_{50} of the Cam3.II parent), with or without an initial period of exposure to QN at 1×
182 IC_{50}, we obtained 33 parasite pools. Those DNAs were then whole-genome sequenced.

183 We also sequenced DNA from mock-treated bulk cultures processed in parallel
184 (**Extended Data 2b,d** and **Table S5**).
185
186 We then compared the genome data of bulk progeny pools from QN-treated parasites vs
187 'no drug timepoint control' or day 0 (D0) control samples. Pairwise comparisons between
188 two different QN selections and their 'D0' controls yielded largely consistent quantitative
189 trait loci (QTLs) (**Extended Data 4**). The comparison using the higher QN concentration
190 (180 nM) yielded a significant chromosome 7 peak, spanning 58 kb, that was located 191
191 kb downstream of *pfcrt* and that was driven by QN-resistant Cam3.II loci (**Table S6**). This
192 58 kb region did not contain any previously known drug resistance markers. These results
193 show the power of bulk segregant analysis as a screening tool to identify regions of
194 interest with multigenic traits. Bulk segregant analysis, however, needs to be followed-up
195 by progeny clone-based QTL analysis to narrow down candidates and reveal epistatic
196 relationships.
197
198 **Progeny clone-based trait mapping identifies novel resistance-associated peaks**
199 **on chromosomes 7 and 12**
200 To further resolve the segments associated with QN resistance, we implemented QTL
201 analysis with individually cloned progeny (**Fig. 2e** and **Table S7**) by measuring their QN
202 IC_{50} and IC_{90} values in 72-hour assays (**Fig. 1c,d** and **Extended Data 5a** and **Table S4**).
203 These phenotypic data were then compared with their whole-genome sequences (**Fig.**
204 **2a,b,d,e** and **Extended Data 5b,c**). As a comparator, we also included CQ and md-CQ.
205
206 For QN, we obtained the highest, statistically significant peaks on chromosomes 7 and
207 12, and several other minor QTLs with lower LOD scores, confirming that QN resistance
208 is multigenic (**Fig. 2a,b,d**). The chromosome 12 QN QTLs either encompassed (IC_{50}) or
209 perfectly matched (IC_{90}) the CQ and md-CQ QTLs. Strikingly, whereas the QN IC_{50}
210 chromosome 7 peak centered close to *pfcrt*, the QN IC_{90} (high-grade resistance) peak
211 was centered 296 kb downstream of *pfcrt* and encompassed 33 genes with
212 nonsynonymous SNPs between the parents (**Fig. 2e** and **Table S7**).
213

214 For md-CQ and CQ, we found two shared major peaks—a chromosome 7 peak harboring
215 *pfcrt* and a chromosome 12 peak that was usually co-inherited with *pfcrt* (i.e. mostly
216 mutant or WT at both loci), with evidence of strong linkage disequilibrium (**Fig. 2c,e** and
217 **Extended Data 5** and **Table S4**). The md-CQ IC_{90} and CQ IC_{50} and IC_{90} chromosome 12
218 peaks consist of 30 genes, of which 10 have nonsynonymous SNPs between the parents.
219 These SNPs were also observed in field populations (**Table S7**). A smaller chromosome
220 6 peak observed with QN and to a marginal extent md-CQ was 245kb (QN IC_{50} and IC_{90}),
221 49kb (md-CQ IC_{50}), or 2kb (md-CQ IC_{90}) away from the *aat1* S258L/F313S variant that
222 was recently proposed to be an additional marker of CQ resistance[38].
223
224 **The chromosome 12 peak harbors *samc*, *thzk*, and *ftsh1* that associate with quinine**
225 **and chloroquine resistance**
226 From amongst the 10 genes on chromosome 12 that harbored point mutations, we
227 selected *samc* (PF3D7_1241600), *ftsh1* (PF3D7_1239700), and *thzk* (PF3D7_1239600)
228 as top candidates (**Fig. 3**) based on their previous associations with *P. falciparum*
229 resistance to antiplasmodial compounds[39-41]. In an earlier transposon mutagenesis
230 screen with *in vitro* cultured *P. falciparum* ABS parasites[42], *samc* was predicted to be
231 essential, whereas *ftsh1* and *thzk* were predicted to be dispensable with either no or slight
232 fitness cost, respectively.
233
234 We also looked for evidence of selective pressures on these genes in *P. falciparum* field
235 isolates, using the Pf3k genome database[43] (**Extended Data 6b-d**). FtsH1 D695G
236 (present in Cam3.II) was observed in Southeast Asia and not in Africa. Haplotypes
237 encoding the SAMC mutations I176K/R (K observed in Cam3.II) and S193A/P/T (A
238 observed in Cam3.II) were prevalent, especially in Southeast Asia. The Cam3.II ThzK
239 A301V mutation was present at low prevalence across Southeast Asian and African
240 countries. One explanation for why these loci would not have been detected in prior CQ
241 QTL analyses with the HB3×Dd2 and 7G8×GB4 genetic crosses is that the *ftsh1, thzk*
242 and *samc* alleles were identical between those parents.
243

244 **FtsH1 mutations can modulate quinine and chloroquine resistance**
245 To directly test whether the chromosome 12 QTL candidates *samc, thzk* or *ftsh1*
246 contribute to QN and CQ resistance, we reverted these mutant alleles to WT in Cam3.II
247 parasites (**Supplemental Fig. 2** and **Tables S8, S9**). We then tested for susceptibility to
248 QN, md-CQ, and CQ in gene-edited lines (denoted as *samc*^{WT}, *thzk*^{WT} or *ftsh1*^{WT})
249 compared to the unedited Cam3.II parent (**Fig. 4a-f** and **Table S10**). *samc*^{WT} and *thzk*^{WT}
250 parasites showed no significant difference to all three drugs when compared to Cam3.II.
251 Also, no shift was observed when introducing the *thzk* A301V mutation into NF54
252 parasites (**Table S10**). In contrast, reverting *ftsh1* to WT in Cam3.II caused a significant
253 decrease in the level of resistance to QN, CQ and md-CQ, with IC_{50} decreases averaging
254 33% to 50%. These results provide evidence that *ftsh1* may act as a potential contributor
255 to QN resistance and mutant *pfcrt*-mediated CQ and md-CQ resistance.
256
257 ***dmt1* is a top candidate for mediating quinine resistance**
258 Of the 82 genes within the QN IC_{90} chromosome 7 QTL segment, 33 harbored
259 nonsynonymous SNPs that were all present only in the QN-resistant Cam3.II parasite but
260 not NF54. Within this segment, DMT1 was of particular interest as it is annotated as a
261 putative drug/metabolite transporter (DMT) that, like PfCRT, is a member of the
262 drug/metabolite exporter (DME) family within the DMT superfamily. This locus began ~4
263 kb downstream of the chromosome 7 QN IC_{90} QTL peak (LOD = 10.4). DMT1 is predicted
264 to be a 434-amino acid-long membrane transporter with 9 or 10 transmembrane domains
265 based on TMHMM and TMpred analyses[44,45], respectively (data not shown), whereas
266 PfCRT has 424 amino acids and ten transmembrane domains. Cam3.II DMT1 harbors
267 Y107N and S129L mutations that are not present in NF54. Our analysis of 2,512 *P.*
268 *falciparum* genomes (in the Pf3k database), covering six Asian and eight African
269 countries, revealed the frequent presence of Y107N in all countries, whereas S129L was
270 only observed in Asia in samples that already harbored Y107N (**Extended Data 6a**).
271
272 Using ChimeraX MatchMaker, we calculated the structural similarity between the
273 AlphaFold-predicted NF54 DMT1[46] and cryo-EM derived 7G8 PfCRT (**Extended Data**
274 **7**)[47]. This comparison revealed similar folds in their respective transmembrane regions,

275 with a good alignment of 1.27 Å between 47 pruned atom pairs that are predicted to be
276 in the transmembrane domains. However, the overall alignment across all 300 atom pairs
277 was poor (20.175 Å) most likely due to the flexible regions that are annotated by
278 AlphaFold as "very low confidence", where the Y107N and S129L mutations reside.
279
280 Sequence alignments with DMT1 orthologs in other *Plasmodium* species revealed strong
281 conservation in the TMHMM-predicted transmembrane domains (**Supplemental Fig. 3a**).
282 Phylogenetic trees (**Supplemental Fig. 3b**) revealed that *P. falciparum* DMT1 was the
283 most similar to DMT1 orthologues in other laverania malaria species, consistent with *P.*
284 *falciparum* originating from gorillas or other great apes[48]. In *P. falciparum*, *dmt1* was
285 predicted to be potentially dispensable in cultured ABS parasites and to have a fitness
286 cost (**Fig. 3a**) in a transposon mutagenesis screen[42], although in the Pf3K genome
287 database no isolates were found to have stop codons, suggesting essentiality *in vivo*.
288
289 **Mutant DMT1 may play a modulatory role in parasite susceptibility to quinine**
290 To experimentally test whether DMT1 is a modulator of QN susceptibility *in vitro*, we
291 applied CRISPR/Cas9-based gene editing (**Supplemental Fig. 2a**) to modify this locus
292 at the Y107 and S129 positions in both parents. Editing was also applied to various
293 progeny (H079, H030, H071, H062, and H046) that were selected to cover a range of QN
294 susceptibilities and genotypes at the *dmt1*, *pfcrt* and *ftsh1* loci (**Table S4**). Editing was
295 confirmed using PCR primers and Sanger sequencing (**Table S8**). We then conducted
296 drug assays on these lines alongside their unedited parasites (**Fig. 5a** and **Table S10**). A
297 statistically significant sensitization to QN was observed between the SNP-edited lines
298 and their unedited parasites only for H079 (mutant for *pfcrt*, *dmt1* and *ftsh1*). There was,
299 however, a trend of the Cam3.II and H071 DMT1 revertants (*dmt1*^{WT}) having a lower QN
300 IC_{50} than the unedited strain (~20% and 19% mean reductions, respectively). In the H062
301 and H046 progeny (both Dd2 PfCRT, WT DMT1), mutating DMT1 did not cause a shift in
302 QN susceptibility. These data suggest that the genetic background, and the specific
303 constellation of how individual modulators including DMT1 are coinherited, play key roles
304 in QN response.
305

306 We also profiled DMT1 SNP-edited lines and unedited isogenic controls against CQ, md-
307 CQ, and the related 4-aminoquinoline md-amodiaquine (md-ADQ) (**Supplemental Fig.**
308 **4a-c** and **Table S10**). No statistically significant differences were observed, except for the
309 H071 isogenic pair. H071 DMT1 revertants became less resistant to CQ and md-CQ than
310 their unedited, CQ-resistant isogenic line, possibly due to an altered interaction with
311 another gene in this recombinant background. The Cam3.II DMT1 revertant parasites did
312 not become less resistant to md-CQ, CQ, and md-ADQ, compared with the isogenic
313 DMT1 mutant lines. These results suggest that the modulatory role of DMT1 is mostly
314 QN-specific.
315
316 **Phenotypic profiling of DMT1 knockout strains validates DMT1 as a marker of**
317 **quinine resistance**
318 To further investigate the role of DMT1, we generated KO parasites in Cam3.II parasites
319 (**Supplemental Fig. 5**). Phenotypic characterization of four DMT1 KO clones, plus
320 parental Cam3.II and NF54 parasites, showed that the DMT1 KO led to 25–30% lower
321 QN IC_{50} and IC_{90} levels in the Cam3.II background (**Fig. 5b** and **Supplemental Fig. 4d**
322 and **Table S10**). These data are consistent with DMT1 contributing to a multifactorial
323 basis of QN resistance. KO parasites showed increased susceptibility to MFQ, LMF, and
324 CQ at the IC_{90} but not IC_{50} level, evoking earlier findings of overlapping mechanisms of
325 parasite susceptibility to these structurally partially related drugs (**Extended Data**
326 **1a**)[8,9,49,50].
327
328 **Gene editing confirms a contribution for mutant PfCRT in QN resistance**
329 Our QTL analysis with QN IC_{50} values revealed a chromosome 7 segment that also
330 included *pfcrt*. To test this association, we reverted the *pfcrt* Dd2 allele in Cam3.II
331 parasites to the WT (NF54) allele, using an established zinc finger nuclease-based gene
332 editing method[51]. Dose-response assays showed a significant reduction in the QN IC_{50},
333 and to a lesser extent QN IC_{90}, values in the Cam3.II genetic background (**Fig. 5c**). Values
334 remained higher than the reference NF54 line, consistent with *pfcrt* being only one
335 component of a multigenic basis of QN resistance. Reversion of mutant *pfcrt* to the WT
336 allele caused Cam3.II parasites to revert to a fully CQ-sensitive phenotype (evident at

337 both IC_{50} and IC_{90} levels; **Fig. 5d**), as expected given the primary role for this gene in
338 mediating CQ resistance.
339
340 **DMT1 localizes to the digestive vacuole, lipid bodies, parasitophorous vacuolar**
341 **membrane, as well as structures associated with vesicular trafficking**
342 To explore the subcellular localization of this novel transporter, we generated DMT1-
343 3×HA-tagged parasites in NF54 parasites (**Supplemental Fig. 6**). Widefield
344 deconvolution confocal microscopy with anti-3×HA antibodies showed a punctate pattern
345 evident in all ABS parasites. We then co-stained parasites with antibodies or dyes specific
346 for specific organelles or subcellular compartments (**Fig. 6a-g** and **Extended Data 8a-i**)
347 and quantified their colocalization with DMT1-3×HA (**Table S11** and **Extended Data 8j**).
348
349 We observed partial colocalization of DMT1 with the DV-resident markers PfCRT and
350 plasmepsin 2 (PfPM2), with mean ± SEM overlap of 29.2 ± 8.0% and 16.7 ± 2.5%,
351 respectively (**Fig. 6f** and **Extended Data 8f,g**). However, the mean colocalization values
352 were not as high for some other organelles, indicating that DMT1 only partially overlapped
353 with the DV membrane. In some parasites DMT1 almost fully (>80%) colocalized with
354 lipid bodies (stained using Nile Red; 43.6 ± 10.8%) (**Fig. 6g** and **Extended Data 8h**), the
355 endoplasmic reticulum (ER) (39.8 ± 10.3%) (**Fig. 6c** and **Extended Data 8d**), and the
356 parasitophorous vacuolar membrane (PVM) (40.9 ± 12.4%) (**Fig. 6e** and **Extended Data**
357 **8e**). In other parasites, however, there was minimal overlap, leading to moderate
358 colocalization values (shown in parentheses when averaged between these two
359 patterns). This discrepancy may be due to DMT1 being trafficked within the parasite.
360 Interestingly, Nile Red has been shown to localize to DV-adjacent small cytoplasmic
361 neutral lipid droplets that contain di- and triacylglycerols in *P. falciparum*, which may
362 explain why we observed colocalization with both Nile Red and PfCRT[52-54]. DMT1 also
363 partially colocalized with Rab5B-positive early endosomes (27.9 ± 7.2%) (**Fig. 6b** and
364 **Extended Data 8c**), and less so with Rab7- positive late endosomes (10.2 ± 5.7%) (**Fig.**
365 **6a**) and Rab11A- positive post-Golgi compartments (10.8 ± 4.5%) (**Extended Data 8i**).
366 These observations suggest a role for DMT1 in vesicular trafficking. DMT1 also showed

367 some colocalization with K13, the ART resistance mediator that is present in cytostomes
368 at the plasma membrane, the ER, and internal vesicular structures[55-57]. DMT1 did not
369 colocalize with the mitochondria or the apicoplast.
370
371 **NF54 and Cam3.II DMT1 isoforms differentially transport [^{3}H]QN**
372 To determine whether DMT1 can transport QN, we purified and reconstituted NF54 (WT)
373 and Cam3.II (Y107N / S129L) DMT1 isoform proteins in proteoliposomes[47] and measured
374 [^{3}H]QN and [^{3}H]CQ uptake (**Fig. 6h,i**). DMT1 isoforms were found to transport both
375 [^{3}H]QN and [^{3}H]CQ, with the mutant Cam3.II isoform showing significantly higher [^{3}H]QN
376 uptake. These data provide a possible mechanistic explanation that links DMT1 as a
377 potential transporter of QN and suggest that the QN mechanism of action and resistance
378 may, in part, be mediated by mutant DMT1-mediated QN transport. For [^{3}H]CQ, the
379 highest level of transport was observed with Cam3.II PfCRT, contrasting with zero
380 detectable transport with NF54 PfCRT. Lower [^{3}H]CQ transport levels were observed with
381 both the Cam3.II and NF54 DMT1 isoforms, consistent with mutant DMT1 being a factor
382 only for QN and not for CQ resistance. Our data agree with previous studies partially
383 associating mutant PfCRT with QN resistance, and observations of PfCRT transporting
384 non-CQ drugs, thereby impacting the parasite drug response by potentially changing the
385 drug concentration at their site of action[58].
386
387 **QN partially inhibits heme detoxification**
388 To evaluate the involvement of QN in heme detoxification, we tested its ability to inhibit
389 conversion of heme to β-hematin (synthetic hemozoin) in a cell-free heme detoxification
390 assay[59,60]. When compared with the known β-hematin inhibitors CQ (mean ± SEM IC_{50} =
391 11.2 ± 0.5 μM) and md-ADQ (mean ± SEM IC_{50} = 5.2 ± 1.0 μM), we observed a lower
392 degree of inhibition with QN (mean ± SEM IC_{50} = 22.1 ± 1.2 μM) and MFQ (mean ± SEM
393 IC_{50} = 33.8 ± 4.6 μM) (**Extended Data 1b** and **Table S12**). These results are consistent
394 with the structural relatedness between QN and MFQ (**Table S13**) and prior evidence of
395 partial involvement of these drugs in the heme detoxification pathway[61,62].
396

397 ## Discussion

398 Here, we report the identification of three genetic markers associated with a polygenic
399 basis of *P. falciparum* ABS parasite resistance to QN, an antimalarial drug first used in
400 the 1600s for which resistance has long been enigmatic. This was achieved using a
401 genetic cross between QN-resistant Cam3.II and QN-sensitive NF54 parasites in a
402 humanized mouse model, from which we recovered progeny representing 120 unique
403 recombinant haplotypes. QTL mapping associated QN resistance with a dominant peak
404 on chromosome 7 that included a previously uncharacterized drug-metabolite transporter,
405 DMT1. A smaller upstream peak aligned with *pfcrt*, the primary determinant of resistance
406 to the former gold standard drug, CQ. For both QN and CQ, we also observed a peak on
407 chromosome 12, including *ftsh1*. Gene editing studies confirmed a role for *dmt1*, *pfcrt* and
408 *ftsh1* in QN resistance, supporting these as candidate molecular markers for malaria
409 molecular surveillance.
410
411 DMT1 is a predicted drug-metabolite exporter that localizes to the DV, lipid bodies, the
412 PVM, and structures associated with vesicular trafficking, as evidenced by partial Rab5B
413 and ER staining. Our results suggest that DMT1 may be trafficked by vesicular structures
414 from the parasitophorous vacuolar membrane to either the DV membrane or DV-adjacent
415 lipid bodies. With the latter, we speculate that DMT1 may be involved in lipid storage of
416 phospholipids that are known to promote β-hematin formation[54,63]. Structurally, DMT1
417 resembles PfCRT, which resides solely on the membrane of the DV wherein heme
418 accumulates and is detoxified via biomineralization of β-hematin dimers into inert
419 hemozoin[26]. We were able to functionally link QN and DMT1 by showing that
420 proteoliposomes loaded with purified recombinant DMT1 protein could mediate [^{3}H]QN
421 uptake, with the Cam3.II variant showing higher levels than the WT protein. These data
422 suggest that mutant DMT1 might contribute to QN resistance via intracellular flux away
423 from this drug's site of action. We note that QN uptake was also observed with mutant
424 PfCRT, more so than with WT PfCRT, suggesting an additional role for PfCRT in QN
425 resistance. Those findings are consistent with gene editing-based evidence that parasites
426 expressing WT PfCRT were more sensitive to QN than the isogenic line expressing
427 Cam3.II PfCRT. The direction of transport is uncertain, as QN can at high concentrations

428 inhibit hemozoin formation that occurs in the DV, yet this drug is also suspected to have
429 additional, unknown targets located in the cytosol[19].
430
431 DMT1 harbors two mutations (Y107N / S129L) in Cam3.II but not NF54. This gene was
432 also WT in prior genetic cross parents, which would explain its prior lack of
433 detection[16,29,38,64]. In cultured parasites, *dmt1* is nonessential and we found that Cam3.II
434 DMT1 KO parasites were significantly sensitized to QN (by ~25% at the IC_{50} level),
435 without affecting parasite susceptibility to other antimalarials (CQ, md-CQ, md-ADQ,
436 MFQ, and LMF). QN resistance, and the contribution of DMT1, remains complex. SNP-
437 edited Cam3.II $DMT1^{WT}$ parasites exhibited a ~17% decreased QN susceptibility
438 compared to their unedited parent, and a 20–40% decrease in two progeny genetic
439 backgrounds, yet none in another. The larger reduction in QN IC_{50} levels in the Cam3.II
440 KO line compared to the SNP-edited line suggests that the level of DMT1 protein
441 expression may also be important for mediating QN resistance. An analogous finding
442 applies to PfCRT, where reducing the protein expression level led to a corresponding
443 reduction in CQ IC_{50} in CQ-resistant parasites[65,66]. Of note, we observed no significant
444 shift in QN response when mutating DMT1 from WT to Y107N / S129L in three genetic
445 backgrounds (NF54, H046 and H062), suggesting that *dmt1* is only one determinant of a
446 multigenic basis of QN resistance that in a background-dependent manner also includes
447 PfCRT.
448
449 Our QTL analyses identified an unexpected peak on chromosome 12 that overlapped for
450 QN, CQ and md-CQ. Gene editing of prioritized candidates implicated *ftsh1* as a potential
451 contributor to these resistance mechanisms, as the Cam3.II *ftsh1* MUT^{WT} parasites
452 (where the D659G mutation was reverted to WT) became significantly more susceptible
453 to all three drugs compared to unedited Cam3.II (**Fig. 4**). This gene encodes a membrane
454 metalloprotease that is homologous to the bacterial membrane AAA+ metalloprotease[67].
455 In *P. falciparum* and *Toxoplasma gondii* (both Apicomplexa), FtsH1 is required for
456 apicoplast biogenesis[39]. In *P. falciparum* D10 parasites, FtsH1 G489C (located in the
457 peptidase domain) confers resistance to actinonin, an antibiotic that kills *P. falciparum*
458 within a single parasite generation – unlike apicoplast ribosome-targeting antibiotics that

459 cause delayed death[41,68]. It remains to be tested whether QN might also interfere with
460 apicoplast biogenesis.
461
462 We observed strong linkage disequilibrium between *ftsh1* and the chromosome 7
463 segment harboring both *pfcrt* and *dmt1*, suggesting functional complementarity that might
464 offset any physiological defects resulting from mutations in *pfcrt* or *dmt1*. A prime
465 candidate is the excess of short globin-derived peptides observed in mutant *pfcrt*
466 parasites[66,69-71]. Metabolomic assays are planned to assess whether peptide levels return
467 to a normal baseline in progeny harboring both chromosome 7 and 12 loci. When
468 considering how FtsH1 might relate to DV transporters, we note that the apicoplast is
469 essential for isoprenoid biosynthesis, which prenylates Rab5 proteins required for vesicle
470 trafficking to the DV and normal DV development[72,73].
471
472 Future studies are required to test for changing prevalences of mutant *dmt1*, *pfcrt*, and
473 *ftsh1* in areas where QN is being used. This will become increasingly important if QN use
474 expands in response to the increasing detection of *P. falciparum* strains across Africa that
475 are partially resistant to artemisinin and the threat that they pose to effective treatment of
476 severe malaria with artemisinin derivatives. Further studies are also required to edit these
477 mutations across additional parasite strains, and further analysis of whether these mutant
478 genes operate epistatically as a complex genetic trait of resistance.
479
480 Lastly, our QN studies highlight the value of treating malarial infections with compounds
481 having complex modes of action that require resistance to be multigenic. Despite QN
482 being the oldest antimalarial drug, it remains broadly effective to this day. In future drug
483 discovery efforts, chemical compounds that have multiple *P. falciparum*-specific targets
484 and/or multiple low-level resistance modulators merit prioritization for clinical use.
485

486 Methods

487 **Parasite *in vitro* culture.** *P. falciparum* ABS parasites were cultured in human RBCs at
488 3% hematocrit, using RPMI 1640 supplemented with 25 mM HEPES, 2.1 g/L sodium
489 bicarbonate, 10 mg/mL gentamicin, 50 mM hypoxanthine, and 0.5% (w/v) AlbuMAX II

490 (Thermo Fisher Scientific). Parasites were maintained at 37°C under 5% O_2/ 5% CO_2/
491 90% N_2 gas conditions. RBCs and human serum were procured from the Interstate Blood
492 Bank (Memphis, TN) and RBCs were also procured from the New York Blood Center
493 (New York, NY).
494
495 **Genomic DNA (gDNA) extraction.** Parasite genomic DNA was obtained from cultures
496 at 5 to 10% parasitemia with mostly trophozoite and schizont stages. RBCs were lysed
497 with 0.1% saponin in 1×PBS and parasite DNA extracted with the QIAamp DNA Blood
498 Midi Kit (Qiagen) using a combined RNase and Proteinase K treatment. DNA
499 concentrations were determined using a NanoDrop and/or the Qubit dsDNA BR assay kit
500 (Thermo Fisher Scientific).
501
502 **Parasite drug-susceptibility assays.** Parasites were synchronized for at least two
503 consecutive ABS cycles prior to starting drug susceptibility assays and at least once a
504 week thereafter, by exposing ABS cultures to 5% D-sorbitol (Sigma) for 15–20 min at
505 37°C to remove mature parasites, followed by a wash step. In drug susceptibility assays,
506 predominantly ring-stage parasites were exposed to a serially diluted range of drug
507 concentrations (twofold, 10-point dilutions for all drugs except for QN that used 12-point
508 dilutions), or 700 nM DHA (kill control), or a no drug control. Assays started at 0.2%
509 parasitemia and 1% hematocrit in 96-well flat-bottom plates incubated at 37°C for 72 h in
510 5% O_2 / 5% CO_2 / 90% N_2. Final parasitemias were measured using an IntelliCyt iQue
511 Screener Plus cytometer (Sartorius), a BD Accuri C6 Plus cytometer with a HyperCyt
512 plate sampling attachment (IntelliCyt), or a BD FACSCelesta flow cytometer with the BD
513 High Throughput Sampler (HTS). Cells were stained with 1×SYBR Green I (Invitrogen)
514 and 100 nM MitoTracker DeepRed FM (Invitrogen) for at least 20 min and diluted in
515 1×PBS prior to sampling (typically ~8,000-10,000 RBCs per well). Parasitemia in each
516 well was determined as the percentage of MitoTracker-positive SYBR Green I-positive
517 infected RBCs within the cell subpopulation gated in the FSC vs SSC plot. Parasitemia
518 was then normalized by subtracting the background parasitemia in the 700 nM DHA kill
519 control, and 50% inhibitory concentration (IC_{50}) and 90% inhibitory concentration (IC_{90})
520 values were calculated by nonlinear regression analysis (Prism version 10, GraphPad).

521 For that analysis, we used a 4-parameter curve fitting where minimum and maximum
522 parasitemias were set to 0% and 100% growth, respectively. Drug susceptibility assays
523 were performed with QN, CQ, md-CQ, md-ADQ, LMF, and MFQ. Statistical significance
524 was determined by nonparametric, two-tailed Mann-Whitney *U*-tests for QN, CQ, and md-
525 CQ QTLs and Student's *t*-tests for all other drug assays (Prism version 10, GraphPad).
526
527 **Genetic cross.** NF54 and Cam3.II *P. falciparum* gametocytes were generated as
528 previously described[33]. Briefly, parasites were propagated in RPMI 1640 media
529 containing 10% (v/v) human serum, at 4% hematocrit and 37°C in a glass candle jar.
530 Cultures were initiated at 0.5% asynchronous asexual parasitemia from a low-passage
531 stock and maintained up to day 18 with daily media changes but without any addition of
532 fresh RBCs. Day 15 to 18 cultures, containing largely mature gametocytes, were used for
533 mosquito feeds. Cultures were centrifuged (108 × g, 4 min) and the parasite pellet was
534 adjusted to 0.3% gametocytemia in a mixture of human O+ RBCs supplemented with
535 50% (v/v) human serum. To conduct a genetic cross between NF54 and Cam3.II, we
536 used a 1:1 ratio of gametocytes at a final gametocytemia of 0.3%. Gametocytes were fed
537 for 1 h to 4–6-day old *Anopheles stephensi* mosquitoes (Liston strain) that had been
538 starved overnight, using glass membrane feeders. Unfed mosquitoes were removed after
539 feeding. Fed mosquitoes were then maintained on a 10% sugar solution at 25°C and 80%
540 humidity with a 14:10 h (light:dark) cycle including a 2 h dawn/dusk transition. Human
541 RBCs used to set up the cultures were collected weekly from healthy volunteers, with
542 informed consent, under a Johns Hopkins University Institutional Review Board approved
543 protocol (number NA_00019050). All experiments were performed in accordance with
544 institutional guidelines and regulations.
545
546 On day 7 post-infected blood meal, mosquito midguts were harvested and stained with
547 mercurochrome. Oocysts were counted by brightfield microscopy using a Nikon E600
548 microscope with a PlanApo 10× objective. We observed a ~85% prevalence of infection,
549 with an average of ~20 oocysts per mosquito. Between days 14 to 16, salivary glands
550 were harvested from ~35 mosquitoes, homogenized and the sporozoites counted using

551 a hemocytometer. On average we obtained 40,000 salivary gland sporozoites per
552 mosquito.
553
554 All animal experiments were performed in accordance with the Animal Care and Use
555 Committee (ACUC) guidelines and approved by the Johns Hopkins ACUC (Protocol
556 M017H325), with modifications to a protocol reported previously[74]. FRG NOD human
557 liver-chimeric (huHep) mice[75] were purchased and shipped from Yecuris Corporation.
558 Upon arrival we began withdrawal of the mice from 2-(2-nitro-4-trifluoromethylbenzoyl)-
559 1,3-cyclohexanedione (NTBC). Mice were housed in a sterile facility with sterile bedding,
560 food, and water. Mice were weighed daily and those that showed weight loss >10%
561 (compared to pre-shipment weight) were treated with 300 μL of sterile saline via
562 intraperitoneal injection and given a nutritional supplement in water (STAT;
563 https://www.prnpharmacal.com/products/nutritional-supplements/stat/). Prior to infection,
564 mice were allowed to recover from shipping for 2 to 3 days. Infection with *P. falciparum*
565 sporozoites was performed either by mosquito bite or by intravenous (IV) inoculation. For
566 the mosquito bite approach, mosquitoes were allowed to probe/feed for 17 to 19 min on
567 mice anaesthetized with 150 μL ketamine/xylazine. Two mice (A and B) each received
568 mosquito bites from approximately 60 mosquitoes. Two other mice (C and D) were given
569 prophylactic penicillin/streptomycin antibiotics and then IV-inoculated with 200,000
570 sporozoites dissected from mosquito salivary glands. Mice infected by mosquito
571 bite remained stable and healthy appearing for the remainder of the experiment. In
572 contrast, both mice infected by IV inoculation lost ~5% of their body weight relative to their
573 pre-shipment weight and were given extra rehydration gel food. On days 5.5 and 6.5 post-
574 sporozoite infection, 450–500 μL of RPMI-washed human RBCs at ~70% hematocrit were
575 IV-inoculated into each mouse (except for an intraperitoneal injection for Mouse B due to
576 scar tissue at the tail vein injection site). Mice were given new dextrose, cages, and
577 rehydration gel food on both days. At day 7 post-infection, ABS parasites were detected
578 at 0.3–0.8% parasitemia and blood was recovered by cardiac puncture of mice
579 anesthetized with ketamine/xylazine (**Table S1**). Bulk freezes were made after one and
580 two cycles in culture. The bulk freezes made after one cycle were thawed from each
581 mouse and used to obtain progeny clones by limiting dilution cloning (referred to as clones

582 from no drug pressure prior to cloning). The post-two cycle freezes for mice B and C were
583 later thawed and pressured at 50 nM or 75 nM CQ, or 75 nM or 95 nM QN, for 3 days in
584 5 mL cultures at 3% hematocrit. Surviving parasites were then cloned and cryopreserved.
585 Mouse B 'no drug', as well as mouse B and C QN 95 nM pre-selected bulks, were thawed
586 and pressured at QN 0 nM, 140 nM (and later 240 nM), or 180 nM (and later 240 nM) for
587 4 days for bulk selection experiments. Drug-pressured bulks were cloned by limiting
588 dilution and cryopreserved.
589
590 **Parasite strains and progeny cloning.** The Cam3.II G8 parasite, shortened throughout
591 as Cam3.II, is a clone of the Cam3.II parasite (also known as RF967 or PH0306-C, kindly
592 provided by Dr. Rick Fairhurst, then at the NIH). NF54 (JHU stock) and Cam3.II parents
593 and their genetic cross progeny were cultured in human RBCs as described above, with
594 the addition of 10% (v/v) human serum. Parasites were maintained at 37°C under 5% O_2/
595 5% CO_2 / 90% N_2 gas conditions. After cloning by limiting dilution, parasites were adapted
596 to media devoid of 10% human serum, and all phenotyping was conducted in serum-free
597 media.
598
599 **Whole-genome sequencing (WGS) of genetic cross progeny pools and clones.**
600 Parasite samples were subjected to WGS using the Illumina Nextera DNA Flex library
601 preparation protocol. Briefly, 150 ng of gDNA was fragmented and tagmented using bead-
602 linked transposons and subsequently amplified by five cycles of PCR to add dual-index
603 adapter sequences to the DNA fragments. The libraries were quantified, pooled, and
604 sequenced on either an Illumina MiSeq using the MiSeq Reagent Kit v3 (paired-end 300
605 bp reads) or a NextSeq 550 system using the High Output Kit (paired-end 150 bp reads).
606
607 Progeny were sequenced either directly (for bulk pools and clones after QN 140 nM, 180
608 nM, and 240 nM pressure) or after clonal recombinants had been identified by
609 microsatellite and SNP genotyping (for clones following no drug pressure or CQ 50 nM,
610 CQ 75 nM, QN 75 nM, or QN 95 nM pressure). The WGS data for the parents and progeny
611 clones are visualized in **Fig. 1b**. Sequence data were aligned to the *P. falciparum* 3D7
612 genome (PlasmoDB version 48) using Burrow-Wheeler Alignment (BWA)[76]. Reads that

613 did not map to the reference genome and PCR duplicates were removed using SAMtools
614 and Picard. The reads were realigned around indels using Genome Analyses Tool Kit
615 (GATK) RealignerTargetCreator and base quality scores were recalibrated using GATK
616 BaseRecalibrator.
617
618 Using SAMtools mpileup, variants were called and filtered based on quality scores
619 (minimum base quality score ≥20, mapping quality >30, read depth ≥5) and multiallelic =
620 FALSE to obtain high-quality SNPs that were annotated with SnpEff[77]. SNPs for highly
621 polymorphic surface antigens and multi-gene families were removed. Homozygous SNPs
622 that differed between the NF54 and Cam3.II parents were retained, defined as having
623 >90% alternate or reference allele frequency for NF54 or Cam3.II, respectively. We then
624 selected one recombinant progeny per haplotype with the best sequencing coverage
625 (lowest % of SNPs classified as heterozygous (allele frequency of >10% and <90%) or
626 missing (no reads or reads that did not pass the variant caller's quality filter, or DP<5)) to
627 create a list of 120 haplotype genomes, alongside the parents. We further culled these
628 loci if >90% of the 120 progeny had either NF54 or Cam3.II calls and were not multi-
629 allelic. We also removed 48 SNPs that were classified as heterozygous or discrepant for
630 NF54 and/or Cam3.II across multiple sequencing runs. This process led us to retain
631 13,116 high quality SNPs that differed between NF54 and Cam3.II.
632
633 Microsatellite sizes in the NF54 and Cam3.II parental strains were identified as described
634 previously[78]. Briefly, to determine the confidence of a microsatellite based on the number
635 of reads, a custom Python script utilizing the pysam module[79] was written to call reads
636 that harbored insertions or deletions at specified genomic loci within the respective
637 windows. Integrative Genomics Viewer was used to verify the data.
638
639 **Identification of unique recombinants**
640 PCR and gel electrophoresis microsatellite genotyping (n=11 markers; **Table S14**) was
641 used to narrow down which of the 175 progeny obtained after no drug pressure were
642 recombinant clones, before their gDNA was whole-genome sequenced. This work yielded
643 162 clonal progeny (listed in **Table S15** and **Table S16**), of which 71 were chosen for

644 WGS analysis. To obtain additional unique recombinants, we also subjected bulk progeny
645 pols from mice B and C to various CQ and QN drug pressures (**Extended Data 2b** and
646 **Table S15**). We applied CQ 50 nM, CQ 75 nM, QN 75 nM, or QN 95 nM for 3 days, while
647 we applied QN 140 nM (and later 240 nM), and QN 180 nM for 4 days on the 'no drug'
648 bulks or the QN 95 nM pre-pressured bulks. After a drug wash-off and a recovery period,
649 we obtained 133 clonal progeny from CQ pressure and an additional 292 from QN
650 pressure. 296 out of 303 progeny obtained after CQ 50 nM, 75 nM and QN 75 nM or 95
651 nM selections were genotyped with nine markers: two sets of three microsatellite markers
652 via multiplexed capillary electrophoresis-based genotyping (**Table S14**), as well as SNPs
653 in *pfcrt* (A220S), *dhfr* (N51) and *pfmdr1* (Y184F). These 9 markers were used to screen
654 for clonal recombinant progeny before a subset of 92 progeny were whole-genome
655 sequenced. As the primary goal of the higher QN concentrations was to recover QN-
656 resistant progeny, we split cloning plates 1:2 for progeny obtained after QN 140 nM, 180
657 nM, or 140+240 nM, and subjected plates to 72 h of 140 nM QN. Surviving resistant
658 parasites then proceeded to WGS analysis for 95 out of 160 progeny. PCR and either
659 fragment analysis or gel electrophoresis-based MS genotyping always correctly predicted
660 the self-fertilized or recombinant status of the progeny, which was also confirmed by
661 WGS.
662
663 To identify which progeny were isogenic and to assign unique haplotypes, WGS results
664 for the 13,116 high quality SNP positions were hierarchically clustered for the parents and
665 clonal progeny by average linkage using Gene Cluster 3.0[80]. The resulting dendrograms
666 were visualized using Java TreeView[81]. The SNP inputs were as follows: NF54 allele = -
667 3, Cam3.II allele = 3, heterozygous or missing = 0. Clustering of the unique recombinant
668 haplotypes and the two parents were also conducted. If isogenic progeny shared the
669 same haplotype, then the sequence for the progeny with the best sequencing data (lowest
670 percentage of mixed and missing SNP calls) was used as the representative haplotype
671 for subsequent clustering analysis.
672
673

674 **Quinine bulk segregant analysis**

675 Recombinant bulk pools from Mouse B and C (with or without prior QN 95 nM drug
676 pressure) for the NF54×Cam3.II cross were used for QN BSA experiments (full sample
677 list detailed in **Table S5**). Bulk pools were pressured for four consecutive days in a 5 mL
678 culture at 3% hematocrit in culture media (as mentioned above) supplemented with 10%
679 (v/v) human serum, starting at 1% total parasitemia. gDNA, used for library preparations
680 and WGS, was harvested before (day 0 control) and after the 4-day selections (changing
681 media every day with drug wash off after four days) at 0 nM, 140 nM, 180 nM, and 240
682 nM QN, and later (day 4+) when there was sufficient genomic material to harvest (~2%
683 parasitemia). The 0 nM no drug control well was set up at the same time as each drug
684 selection, to ensure drug-specific killing of the pressured well and to harvest no drug
685 control gDNA at the same timepoint as its corresponding drug-pressured well. This 'no
686 drug timepoint' control was used to account for allele frequency changes due to *in vitro*
687 culture alone.

688

689 The gDNA from of the 33 bulk pool samples (**Table S5**) was whole-genome sequenced
690 and used for the QN bulk segregant analysis performed with the R package, QTLseqr[82].
691 As some WGS data from gDNA bulk cultures exhibited low coverage compared to the
692 progeny clones, we used all 106,316 SNPs that distinguished the two parents. SNPs were
693 then filtered using the filterSNPs function[82] using the following restrictions: 0.1≤ reference
694 allele frequency ≤0.9 to remove over- and under-represented SNPs in both bulks,
695 (minimum total depth = 10) / (maximum total depth = 200) and minimum sample depth =
696 5 to filter extremely low and high coverage SNPs in both bulks and in each bulk
697 separately, respectively. SNPs were also removed if there was ≥100 read depth
698 difference between bulks. QTLs were identified by comparing QN-pressured bulks with
699 control bulks using the QTL-seq and G' approaches[83,84]. A window size of 100 kb was
700 used (unless indicated otherwise for G' analysis) to calculate the tricube-smoothed
701 Δ(SNP-*index*) and G statistic (or G') for each SNP within that widow. For the G' analysis,
702 outlier regions were filtered based on Hampel's rule and QTLs were identified as regions
703 with False Discovery Rate (Benjamini-Hochberg-adjusted *p*-values or *q*-values) <0.01.

704 For the Δ(SNP-*index*) analysis, QTLs were identified as regions that pass the 95% and
705 99% confidence intervals.
706
707 **Progeny clone-based quantitative trait locus (QTL) mapping.** The R package, R/qtl
708 version 2[85] was used to map QTL peaks (**Fig. 2** and **Extended Data 5b,c**), using progeny
709 IC_{50} and IC_{90} values as "phenotypes" (**Fig. 1 c-e** and **Extended Data 5a** and **Table S4**)
710 and their WGS data as "genotypes." To identify significant QTLs for each drug response
711 phenotype, 1,000 permutations of phenotypic data (IC_{50}, IC_{90}) were performed to obtain
712 a distribution of maximum Log of the Odds (LOD) scores. These LOD scores were then
713 used to calculate the LOD threshold at 95% probability. Fine mapping of the QTL
714 segments was performed using Bayesian interval mapping at a 95% confidence level.
715 Significant QTL segments are listed in **Fig. 2e**, and the genes within these segments are
716 shown in **Table S7**.
717
718 **CRISPR/Cas9 plasmid construction.** The DMT1 (PF3D7_0715800) Y107N/S129L
719 mutation or WT with binding-site mutations was introduced into the cross parents (NF54,
720 Cam3.II) and five progeny (B-QN95-140-A5, B-CQ75-1-H9, B4-5, B5-4, Clow6, C-QN95-
721 180-F8) using an all-in-one CRISPR/Cas9 plasmid (pDC2-co*Sp*Cas9-h*dhfr*[86]). The *P.*
722 *falciparum* codon-optimized Cas9 endonuclease was derived from *Streptococcus*
723 *pyogenes* and was expressed under a *calmodulin* promoter. The plasmid also carried a
724 human dihydrofolate reductase (h*dhfr*) selectable marker (conferring resistance to the
725 antifolate WR99210) under a *P. chabaudi dhfr-ts* (*Pcdt*) promoter and a *U6* promoter for
726 expressing the guide RNA (gRNA). The DMT1 WT and Y107N/S129L donors were
727 synthesized in a pUC-GW-*amp* vector (Genewiz), with both donors also containing the
728 same three silent (synonymous) mutations at the gRNA recognition site (referred to herein
729 as binding-site mutations or bsmut). These mutations prioritized the PAM and/or the
730 "seed" region <12 nt upstream of the PAM to prevent Cas9 endonuclease-mediated re-
731 cleavage of the donor or the edited recombinant locus. Donors were PCR amplified from
732 the pUC-GW-*amp* vector and subcloned by In-Fusion cloning into pDC2-co*Sp*Cas9-h*dhfr*
733 at the *Eco*RI and *Aat*II restriction sites. A gRNA was selected using ChopChop version
734 3[87] and Benchling (https://www.benchling.com), as close as possible to the mutation site,

735 avoiding poly-T stretches of >3 Ts as they may cause premature transcription
736 termination[88], and prioritizing gRNAs with low off-target scores and at least 3 to 4
737 mismatches to other sites in the genome that are preferably in the PAM and/or the "seed"
738 region. Double-stranded gRNA blocks were synthesized as single-stranded DNA
739 (Eurofins Genomics) and then phosphorylated, annealed, and cloned into the *Bbs*I
740 restriction sites of pDC2-co*Sp*Cas9-h*dhfr* by T4 DNA ligase cloning.
741
742 CRISPR/Cas9 was also used to generate Cam3.II parasites with WT ThzK
743 (PF3D7_1239600) or the A301V mutant, WT FtsH1 (PF3D7_1239700) or the D695G
744 mutant, and WT SAMC (PF3D7_1241600) or the I176K/S193A variant. Donors were
745 synthesized in the pUC-GW-*amp* vector as described above with synonymous binding
746 site (bsmut) mutations introduced for each gene for each of two separate gRNAs. The
747 donors for ThzK and FtsH1 were subcloned into pDC2-co*Sp*Cas9-h*dhfr* as described
748 above while the donor for SAMC was kept in the pUC-GW-*amp* vector and co-transfected
749 instead due to the low complexity of *samc*. Two gRNAs per gene were cloned into the
750 *Bbs*I restriction sites to generate two separate plasmids for each gene, as described
751 above.
752
753 To generate a PfNF54 DMT1 3' 3×human influenza hemagglutinin-based (HA) tagged
754 parasite, a DMT1 donor with a homology region (HR) 1 (342 bp), recodonized 3' end of
755 DMT1 to disrupt homology with no stop codon (165 bp), spacer (6 bp), 3×HA tag with a
756 stop codon, and 3' untranslated region (UTR) HR2 (509 bp) was synthesized in a pUC-
757 GW-*amp* vector (Genewiz), PCR amplified and cloned by In-Fusion cloning into the
758 *Eco*RI/*Aat*II restriction sites of the pDC2-co*Sp*Cas9-h*dhfr* vector. Three gRNAs within the
759 recodonized region were selected and cloned into the vector.
760
761 To generate a Cam3.II DMT1 KO using CRISPR/Cas9 gene editing, 1202 bp out of the
762 1305 bp-long native PfDMT1 exon was replaced with a selectable marker cassette
763 expressing h*dhfr* under the control of the *PcDT* promoter and a 3' UTR from *hrp2*. Human
764 *dhfr* expression was selected using 2.5 nM WR99210. The left homology (499 bp) and
765 right homology (437 bp) regions were PCR amplified from Cam3.II gDNA and inserted by

766 In-Fusion cloning into the *Eco*RI/*Aat*II and *Apa*I restriction sites of the pDC2-co*Sp*Cas9-
767 h*dhfr* vector, respectively. Three gRNAs within the deleted *dmt1* sequence were selected
768 and cloned into the vector.
769
770 All final plasmids were purified using the NucleoBond Xtra Maxi kit (Macherey-Nagel) and
771 confirmed by restriction digests and Sanger sequencing and are listed in **Table S9**.
772 Primers used for cloning and verification are described in **Table S8**.
773
774 **Parasite transfections.** ABS parasites were electroporated with purified circular plasmid
775 DNA as described[89]. Per transfection, a 2.5 mL culture of 3% hematocrit, >5% ring-stage
776 parasites was harvested and washed with 15 mL of 1× Cytomix. 75 μL of parasitized
777 RBCs was then added to 50 μg of plasmid DNA and 1× Cytomix to a total volume of 440
778 μL, transferred to a 0.2 cm cuvette (Bio-Rad), and electroporated at a voltage of 0.31 kV
779 and capacitance of 950 μF using a Gene-Pulser (Bio-Rad)[90]. For SAMC SNP editing, we
780 cotransfected 50 μg each of pUC-GW with donor and CRISPR/Cas9 plasmid with one
781 gRNA; for DMT1 KO, DMT1-3×HA, FtsH1 SNP, and ThzK SNP gene editing, we
782 cotransfected 50 μg each of CRISPR/Cas9 all-in-one plasmids that contained the same
783 donor but two distinct gRNAs. Electroporated cells were transferred from the cuvette to a
784 well in a 6-well plate containing 3% hematocrit blood + media mixture, and media was
785 generally changed ~3–4 h post-transfection (or sometimes ~15 h later). Starting the day
786 after the transfections, the cultures were maintained in 2.5 nM WR99210 (if parasites
787 have triple *dhfr* mutations; N51I/C59R/S108N) or 1 nM WR99210 (if WT *dhfr*) for six
788 consecutive days[91]. WR9210 was procured from Jacobus Pharmaceuticals. Successful
789 gene editing was assessed via Sanger sequencing of PCR products amplified directly
790 from bulk cultures or from bulk culture gDNA. DMT1-3×HA-tagged parasite clones were
791 obtained by limiting dilution. Successful *dmt1*-3×HA tagging was confirmed via PCR,
792 Sanger sequencing, immunofluorescence, and Western blot assays. Successful *dmt1* KO
793 was confirmed by PCR, Sanger sequencing, and gel electrophoresis. Oligonucleotide
794 primers used in this study are listed in **Table S8**.
795

796 **Western blot confirmation of DMT1-3×HA tagging**

797 Western blots were performed with lysates from NF54 DMT1-3×HA-tagged parasites and
798 NF54 PRELI-3×HA-tagged parasites (positive control). Parasite cultures were washed
799 twice in cold 1×PBS, and parasites were isolated by treatment with 0.05% saponin in
800 PBS. Released parasites were lysed in 4% SDS, 0.5% Triton X-100 and 0.5% PBS
801 supplemented with 1×protease inhibitors (Halt Protease and Phosphatase Inhibitor
802 Cocktail, Thermo Scientific) and Pierce Universal Nuclease for Cell Lysis (Thermo
803 Scientific). Samples were centrifuged at 14,000 rpm for 10 min to pellet cellular debris.
804 4×Laemmli Sample Buffer (Bio-Rad) was added to lysates and samples were denatured
805 at 50°C for 15 min (without boiling to prevent aggregation of the DMT1 transmembrane
806 protein). Proteins were electrophoresed on precast 4–20% Tris-Glycine gels (Bio-Rad)
807 and transferred onto nitrocellulose membranes. Western blots were probed with a 1:1,000
808 dilution of primary antibodies to HA (mouse mAb; Cell Signaling), followed by a 1:5,000
809 dilution of anti-mouse IgG H&L HRP-conjugated secondary antibodies (Abcam). Western
810 blots were revealed using Pierce ECL Western Blotting Substrate (Thermo Scientific) and
811 imaged on a ChemiDoc system (Bio-Rad).

812

813 **Indirect immunofluorescence assays (IFAs).** Harvested NF54 DMT1-3×HA-
814 parasitized RBCs were washed twice in 1×PBS and fixed in methanol-free 4% (v/v)
815 formaldehyde (Pierce), supplemented with 0.0075% (v/v) glutaraldehyde (Electron
816 Microscopy Sciences) in 1×PBS for 30 min at room temperature while stationary, followed
817 by one 1×PBS wash. For mitochondria staining, harvested parasites were washed once
818 with pre-warmed RPMI, stained with 50 nM MitoTracker Red CMXRos (Invitrogen) at
819 37°C in the incubator while stationary prior to the 1×PBS wash and fixation, and were
820 kept covered throughout. Cell membranes were then permeabilized in 0.1% Triton X-100
821 in 1×PBS for 30 min at room temperature while stationary, followed by three 1×PBS
822 washes. Autofluorescence was quenched using 0.1 M glycine in 1×PBS for 15 min at
823 room temperature while rotating. Blocking was performed with 3% (w/v) bovine serum
824 albumin (BSA) and 0.1% Tween 20 (v/v) in 1×PBS overnight at 4°C while rotating. Cells
825 were incubated with primary antibodies for 2–4 h at room temperature while rotating, with

826 dilutions ranging from 1:50 to 1:200, followed by a 1 h incubation with a species-specific
827 fluorophore-conjugated secondary antibody diluted in 3% BSA and 0.1% Tween 20 in
828 1×PBS. As primary antibodies, we used rabbit anti-binding immunoglobin protein (BiP)
829 (1:200) (kindly provided by Min Zhang), mouse anti-PfK13 (1:100) (clone E3[56]), rabbit
830 anti-Rab11A, rat anti-Rab5B or -Rab7 (1:50) (kindly provided by Dr. Gordon Langsley),
831 rabbit anti-PfACP (1:200) (kindly provided by Dr. Geoff McFadden), Nile Red (2.5 μg/mL)
832 (Invitrogen), rabbit anti-PfEXP2 (1:200) (MR4), mouse anti-PfCRT (1:200) (clone 2[92]),
833 and rabbit anti-plasmepsin 2 (PM2) (1:100) (BEI Resources). For primary antibodies
834 raised in rabbits, we used Alexa Fluor Plus 594-conjugated goat anti-rabbit IgG (H+L)
835 secondary (1:3000) (Invitrogen). For mouse primary antibodies, Alexa Fluor 594-
836 conjugated goat anti-mouse secondary (1:2000) (Invitrogen) were used. For assays with
837 rat primary antibodies, we used Alexa Fluor 594-conjugated goat anti-rat secondary
838 (1:2000) (Invitrogen). Rat anti-HA (1:2000) (Millipore Sigma) and Alexa Fluor 488-
839 conjugated goat anti-rat secondary (1:2000) (Invitrogen) antibodies were used to test for
840 DMT1-3×HA expression. Samples were also costained with MitoTracker Red CMXRos,
841 Nile Red, or primary antibodies raised in mice or rabbits. Mouse anti-HA (1:100) (Cell
842 Signaling) and Alexa Fluor 488-conjugated goat anti-mouse secondary (1:1000)
843 (Invitrogen) antibodies were used to probe for DMT1-3×HA in co-stains with primary
844 antibodies raised in rats.
845
846 Thin blood smears of stained RBCs were prepared on microscope slides and mounted
847 with high-performance/high-tolerance cover slips (Zeiss) using ProLong Diamond
848 Antifade Mountant with DAPI (Invitrogen) pre-warmed to room temperature. Mounted
849 samples were cured overnight and were imaged using a Nikon TiE Eclipse inverted
850 microscope with a Nikon A1 scanning confocal with a GaAsP spectral detector, and a CFI
851 Plan Apochromat Lambda oil immersion objective with 100× magnification (1.45
852 numerical aperture). 0.2 μm step size Z-stacks were taken for each parasitized RBC. NIS-
853 Elements version 5.02 (Nikon) was used to control the microscope and camera and crop
854 images. Imaris version 9 (Oxford Instruments) was used to perform deconvolution using
855 5 (for DAPI) or 10 (for HA tags and parasite proteins) iterations of the Richardson-Lucy
856 algorithm for each image and quantify colocalization of the deconvolved Z-stacks using

857 the Colocalization Module. Trophozoite-stage parasites were used to quantify
858 colocalization of DMT1 with organelles, as there was more spatial distribution of
859 organelles than in rings and trophozoites were less prone to variability than the
860 multinucleated schizonts. Statistical analyses were performed with Prism version 10
861 (GraphPad). Fiji[93] version 2.11.0 (ImageJ) was used to adjust brightness and contrast,
862 overlay channels, and prepare montages. For 3D rendering of the deconvolved images,
863 we used the Imaris software.
864
865 **Sequence alignment.** The DMT1 protein sequence for the *P. falciparum* NF54
866 (PF3D7_0715800) strain and the orthologous DMT1 sequences from reference strains of
867 *P. reichenowi* (PRCDC_0713100), *P. adleri* (PADL01_0713800), *P. gaboni*
868 (PGSY75_0715800), *P. vivax* (PVP01_1424900), *P. knowlesi* (PKNH_1424800), *P. ovale*
869 (PocGH01_14032100), *P. malariae* (PmUG01_14040800), *P. cynomolgi*
870 (PcyM_1426000), *P. chabaudi* (PCHAS_1423900), *P. berghei* (PBANKA_1422100), *P.*
871 *yoelii* (PY17X_1424100), and *P. gallinaceum* (PGAL8A_00520500) were obtained from
872 the PlasmoDB.org database[94]. Clustal Omega[95], which uses the HHalign algorithm, was
873 used to perform multiple sequence alignments and generate phylogeny trees
874 (**Supplemental Fig. 3**). EMBOSS Needle, which uses the Needleman-Wunsch algorithm,
875 was used to perform global pairwise sequence alignments and calculate the percentage
876 of positions in the alignment that are identical[96]. Both bioinformatic tools were accessed
877 through EMBL-EBI[97].
878
879 **DMT1 NF54 and Cam3.II protein expression and purification, and QN and CQ**
880 **transport measurements.** The NF54 (QN- and CQ-sensitive) and Cam3.II (QN- and CQ-
881 resistant) variants of the DMT1 and PfCRT proteins as well as control Band 3 protein
882 (anion transport control) were expressed, purified, and reconstituted in preformed
883 liposomes as described previously[47], with some modifications. The full-length NF54 and
884 Cam3.II *pfdmt1* were cloned into pEG BacMam vector[98] with the C-terminal tobacco etch
885 virus protease cleavage site (ENLYFQSYV) and a decahistidine affinity tag followed by a
886 streptavidin affinity tag (WSHPQFEK).
887

888 For protein expression, the NF54 and Cam3.II bacmid and baculovirus were generated
889 using a BacMam method[98]. The baculoviruses were produced in Sf9 cells (Expression
890 System) and added to HEK293 GnTi$^-$ cells (ATCC, CRL-3022) incubated at 37°C for 20–
891 24 h in the presence of 5% CO_2 and 60% humidity. We then added 10 mM sodium
892 butyrate (Sigma-Aldrich) and further incubated at 37°C for 48 h before harvesting them.
893 Cell pellets were homogenized in low-salt buffer (10 mM HEPES pH 7.5, 10 mM KCl, 10
894 mM $MgCl_2$, 0.5 mM PMSF, cOmplete EDTA-free protease inhibitor cocktail, 10 μg/mL
895 DNase I, and 8 μg/mL RNase) in a glass homogenizer. Membrane fractions were isolated
896 by ultracentrifugation at 134,000 × g in a type 45 Ti rotor (Beckman Coulter). Membrane
897 fractions were further homogenized and washed twice with high-salt buffer (10 mM
898 HEPES pH 7.5, 10 mM KCl, 10 mM $MgCl_2$, 1 M NaCl, 0.5 mM PMSF, cOmplete EDTA-
899 free protease inhibitor cocktail, 10 μg/mL DNase I, and 8 μg/mL RNase) in a glass
900 homogenizer followed by ultracentrifugation. The membrane fractions were homogenized
901 and solubilized for 2 h in a buffer containing 20 mM HEPES pH 7.5, 200 mM NaCl, 0.5
902 mM PMSF, cOmplete EDTA-free protease inhibitor cocktail, and 1% n-dodecyl-β-d-
903 maltopyranoside DDM/ 0.1% cholesteryl hemisuccinate (CHS). Insoluble material was
904 removed by ultracentrifugation at 134,000 × g for 30 min. The supernatant was added to
905 pre-equilibrated Ni^{2+}-NTA resin (Qiagen) in the presence of 20 mM imidazole, and
906 incubated at 4°C overnight with gentle rotation. The protein-bound resin was washed with
907 10 column volumes of buffer containing 20 mM HEPES pH 7.5, 200 mM NaCl, 60 mM
908 imidazole, 0.1% DDM/ 0.01% CHS. The protein was eluted in buffer consisting of 20 mM
909 HEPES pH 7.5, 200 mM NaCl, 200 mM imidazole, and 0.05% DDM/ 0.005% CHS. The
910 eluted protein was further purified by loading on a Superdex 200 Increase 10/300 GL
911 size-exclusion column (Cytiva Life Sciences) equilibrated with a buffer containing 20 mM
912 HEPES pH 7.0, 150 mM NaCl, and 0.025% DDM/ 0.0025% CHS. Purified proteins were
913 reconstituted in preformed liposomes made of total *E. coli* lipids:cholesteryl
914 hemisuccinate 97:3 (w/w) at a protein-to-lipid ratio of 1:150 (w/w). The lumen of the
915 proteoliposomes was composed of 100 mM KPi, pH 7.5, and 2 mM β-mercaptoethanol.
916 Uptake of [^{3}H]-CQ (300 nM, 1 Ci/mmol) or [^{3}H]-QN (300 nM, 1 Ci/mmol) was measured
917 after diluting PfCRT, DMT1, or Band 3-containing proteoliposomes in 50 μl of 100 mM
918 Tris/MES, pH 5.5 in the presence or absence of the indicated compounds. Band 3 was

919 used as a negative control, for which we expected no or minimal CQ and QN uptake. The
920 protein-specific uptake (pmol/mg) was determined by subtracting the time-dependent
921 accumulation of the tested compounds in control liposomes (lacking PfCRT, DMT1 or
922 Band 3) from the accumulation measured in proteoliposomes containing one of these
923 proteins. Data were collected in three independent experiments, performed in duplicate,
924 and are represented as the mean ± SEM uptake at each timepoint.
925
926 **β-hematin inhibition assays.** A solution containing deionized H_2O/ 305.5 mM lipophilic
927 detergent NP-40 Surfact-Amps Detergent solution (ThermoFisher Scientific)/ dimethyl-
928 sulfoxide (DMSO) was prepared at a v/v ratio of 70%/ 20%/ 10%, respectively, and 100
929 μL was added to columns 1–11 of a flat-bottomed 96-well plate. Working stocks of test
930 and control compounds were constituted to 20 mM (5mM for md-ADQ), from which 20 μL
931 (80 μL for md-ADQ) of each was added to wells in duplicate in column 12 together with
932 deionized H_2O (140 μL; 80 μL for md-ADQ) and 305.5 mM NP-40 detergent (40 μL). This
933 effectively lowered the final drug concentration to 2 mM. Each compound (100 μL) was
934 then serially diluted from columns 12 to 2 (column 1 served as a blank). A 25 mM hematin
935 stock solution was prepared by sonicating hemin (Sigma Life Sciences) in DMSO for 3min
936 and 178.8 μL of this solution was suspended in 20 mL of acetate buffer (1 M, pH 4.8)
937 (made with sodium acetate (Sigma Aldrich) and acetic acid (Fisher Scientific)) and
938 thoroughly mixed. The homogenous suspension (100 μL) was then added to all wells to
939 give a final 0.5 M buffer and 100 mM hematin concentration, as well as a 0.5 mM drug
940 concentration in column 12. Plates were covered and incubated at 37°C for 5 h after which
941 32 μL of a 50% pyridine solution (20% (v/v) H_2O, 20% (v/v) acetone, 10% (v/v) 2 M
942 HEPES buffer (pH 7.4) and 50% (v/v) pyridine (Sigma Aldrich)) was added to each well.
943 60 μL of acetone was then added to each well to assist with hematin dispersion.
944 Unreacted hematin was quantified using the pyridine ferrihemochrome method[99], which
945 relies on aqueous pyridine specifically forming a low-spin complex with hematin but not
946 β-hematin and the complex having an absorbance at 405 nm. The UV-vis absorbance of
947 each well was read at 405 nm on a SpectraMax P340 plate reader. The β-hematin IC_{50}

values for each compound were calculated from the absorbance values at 405 nm using sigmoidal dose-response curve fitting analysis (Prism version 10, GraphPad).

Data and materials availability. All data needed to evaluate the conclusions in the paper are present in the paper and/or the Supplementary Materials. Raw reads of WGS data used in this study have been deposited in NCBI Sequenced Read Archive (SRA) under the BioProject accession number PRJNA1207213.

Acknowledgments

Funding for this work was kindly provided by the National Institute of Allergy and Infectious Diseases, National Institutes of Health (R37 AI050234 and R01 AI185559 to D.A.F.; R01 AI147628 to F.M., M.Q. and D.A.F.; R01 AI132359 to P.S.) and the Bill & Melinda Gates Foundation (OPP1201387 to D.A.F. and P.S.). M.K. gratefully acknowledges funding support from the Japan Student Services Organization and a scholarship from the New York Hideyo Noguchi Memorial Society. S.M. gratefully acknowledges funding support Human Frontiers Science Program Long-Term Fellowship (LT000976/2016-L) and the NIH (R01 AI182318). M.S. was a recipient of a Johns Hopkins Provost's Postdoctoral Fellowship. J.L.S-S gratefully acknowledges support from the NIH (K08AI163497) and from a Doris Duke Physician Scientist Award and a Louis V. Gerstner, Jr. Scholar Award. We also thank Bloomberg Philanthropies for their support of the Johns Hopkins Malaria Research Institute and the Insectary Core Facilities. The IFA studies used the resources of the Herbert Irving Comprehensive Cancer Center Confocal and Specialized Microscopy Shared Resource, funded in part through NIH/NCI Cancer Center Support Grant P30 CA013696, and with the assistance of Drs. Haojie Ji and Theresa Swayne. Brian Kloss and Renato Bruni of the New York Structural Biology Center kindly generated the DMT1 bacmids and viruses for the transport studies. We thank Susan Wyllie and Victor Corpas Lopez (University of Dundee, UK) for their kind help with this project. We dedicate this manuscript to Dr. Leila S. Ross, a brilliant scientist who recently passed away after a heroic battle with cancer.

References

1. World Health Organization. World malaria report 2024. 283 (2024).
2. Dhorda, M. *et al.* Artemisinin-resistant malaria in Africa demands urgent action. *Science* **385**, 252-254 (2024).
3. Ishengoma, D.S. *et al.* Urgent action is needed to confront artemisinin partial resistance in African malaria parasites. *Nat Med* **30**, 1807-1808 (2024).
4. Okombo, J. & Fidock, D.A. Towards next-generation treatment options to combat *Plasmodium falciparum* malaria. *Nat Rev Microbiol* **23**, 178-191 (2024).
5. D'Alessandro, U. *et al.* Treatment of uncomplicated and severe malaria during pregnancy. *Lancet Infect Dis* **18**, e133-e146 (2018).
6. Achan, J. *et al.* Quinine, an old anti-malarial drug in a modern world: role in the treatment of malaria. *Malar J* **10**, 144 (2011).
7. Saeheng, T. & Na-Bangchang, K. Clinical pharmacokinetics of quinine and its relationship with treatment outcomes in children, pregnant women, and elderly patients, with uncomplicated and complicated malaria: a systematic review. *Malar J* **21**, 41 (2022).
8. Cowman, A.F., Galatis, D. & Thompson, J.K. Selection for mefloquine resistance in *Plasmodium falciparum* is linked to amplification of the *pfmdr1* gene and cross-resistance to halofantrine and quinine. *Proc Natl Acad Sci USA* **91**, 1143-7 (1994).
9. Reed, M.B., Saliba, K.J., Caruana, S.R., Kirk, K. & Cowman, A.F. Pgh1 modulates sensitivity and resistance to multiple antimalarials in *Plasmodium falciparum*. *Nature* **403**, 906-909 (2000).
10. Sidhu, A.B., Verdier-Pinard, D. & Fidock, D.A. Chloroquine resistance in *Plasmodium falciparum* malaria parasites conferred by *pfcrt* mutations. *Science* **298**, 210-213 (2002).
11. Ferdig, M.T. *et al.* Dissecting the loci of low-level quinine resistance in malaria parasites. *Mol Microbiol* **52**, 985-97 (2004).
12. Nkrumah, L.J. *et al.* Probing the multifactorial basis of *Plasmodium falciparum* quinine resistance: evidence for a strain-specific contribution of the sodium-proton exchanger PfNHE. *Mol Biochem Parasitol* **165**, 122-31 (2009).
13. Sanchez, C.P. *et al.* A HECT ubiquitin-protein ligase as a novel candidate gene for altered quinine and quinidine responses in *Plasmodium falciparum*. *PLoS Genet* **10**, e1004382 (2014).
14. Dziekan, J.M. *et al.* Identifying purine nucleoside phosphorylase as the target of quinine using cellular thermal shift assay. *Sci Transl Med* **11**, eaau3174 (2019).
15. Tinto, H. *et al.* Relationship between the *pfcrt* T76 and the *pfmdr-1* Y86 mutations in *Plasmodium falciparum* and *in vitro*/*in vivo* chloroquine resistance in Burkina Faso, West Africa. *Infect Genet Evol* **3**, 287-92 (2003).
16. Sa, J.M. *et al.* Geographic patterns of *Plasmodium falciparum* drug resistance distinguished by differential responses to amodiaquine and chloroquine. *Proc Natl Acad Sci USA* **106**, 18883-18889 (2009).
17. Patel, J.J. *et al.* Chloroquine susceptibility and reversibility in a *Plasmodium falciparum* genetic cross. *Mol Microbiol* **78**, 770-87 (2010).
18. Veiga, M.I. *et al.* Globally prevalent PfMDR1 mutations modulate *Plasmodium falciparum* susceptibility to artemisinin-based combination therapies. *Nat Commun* **7**, 11553 (2016).

19. Wicht, K.J., Mok, S. & Fidock, D.A. Molecular mechanisms of drug resistance in *Plasmodium falciparum* malaria. *Annu Rev Microbiol* **74**, 431-454 (2020).
20. Takala-Harrison, S. & Laufer, M.K. Antimalarial drug resistance in Africa: key lessons for the future. *Ann NY Acad Sci* **1342**, 62-7 (2015).
21. Ehrlich, H.Y., Jones, J. & Parikh, S. Molecular surveillance of antimalarial partner drug resistance in sub-Saharan Africa: a spatial-temporal evidence mapping study. *Lancet Microbe* **1**, e209-e217 (2020).
22. Asua, V. *et al.* Changing pevalence of potential mediators of aminoquinoline, antifolate, and artemisinin resistance across Uganda. *J Infect Dis* **223**, 985-994 (2021).
23. Wang, P., Read, M., Sims, P.F. & Hyde, J.E. Sulfadoxine resistance in the human malaria parasite *Plasmodium falciparum* is determined by mutations in dihydropteroate synthetase and an additional factor associated with folate utilization. *Mol Microbiol* **23**, 979-86 (1997).
24. Cowman, A.F., Morry, M.J., Biggs, B.A., Cross, G.A. & Foote, S.J. Amino acid changes linked to pyrimethamine resistance in the dihydrofolate reductase-thymidylate synthase gene of *Plasmodium falciparum*. *Proc Natl Acad Sci USA* **85**, 9109-13 (1988).
25. Peterson, D.S., Walliker, D. & Wellems, T.E. Evidence that a point mutation in dihydrofolate reductase-thymidylate synthase confers resistance to pyrimethamine in *falciparum* malaria. *Proc Natl Acad Sci USA* **85**, 9114-8 (1988).
26. Fidock, D.A. *et al.* Mutations in the *P. falciparum* digestive vacuole transmembrane protein PfCRT and evidence for their role in chloroquine resistance. *Mol Cell* **6**, 861-871 (2000).
27. Brenneman, K.V. *et al.* Optimizing bulk segregant analysis of drug resistance using *Plasmodium falciparum* genetic crosses conducted in humanized mice. *iScience* **25**, 104095 (2022).
28. Mok, S. *et al.* Mapping the genomic landscape of multidrug resistance in *Plasmodium falciparum* and its impact on parasite fitness. *Sci Adv* **9**, eadi2364 (2023).
29. Button-Simons, K.A. *et al.* The power and promise of genetic mapping from *Plasmodium falciparum* crosses utilizing human liver-chimeric mice. *Commun Biol* **4**, 734 (2021).
30. Amaratunga, C. *et al.* Artemisinin-resistant *Plasmodium falciparum* in Pursat province, western Cambodia: a parasite clearance rate study. *Lancet Infect Dis* **12**, 851-8 (2012).
31. Straimer, J. *et al.* K13-propeller mutations confer artemisinin resistance in *Plasmodium falciparum* clinical isolates. *Science* **347**, 428-431 (2015).
32. Sidhu, A.B. *et al.* Decreasing *pfmdr1* copy number in *Plasmodium falciparum* malaria heightens susceptibility to mefloquine, lumefantrine, halofantrine, quinine, and artemisinin. *J Infect Dis* **194**, 528-35 (2006).
33. Tripathi, A.K., Mlambo, G., Kanatani, S., Sinnis, P. & Dimopoulos, G. *Plasmodium falciparum* gametocyte culture and mosquito infection through artificial membrane feeding. *J Vis Exp* **161**, 10.3791/61426 (2020).
34. Jiang, H. *et al.* High recombination rates and hotspots in a *Plasmodium falciparum* genetic cross. *Genome Biol* **12**, R33 (2011).

35. Miles, A. *et al.* Indels, structural variation, and recombination drive genomic diversity in *Plasmodium falciparum*. *Genome Res* **26**, 1288-1299 (2016).
36. Ranford-Cartwright, L.C. & Mwangi, J.M. Analysis of malaria parasite phenotypes using experimental genetic crosses of *Plasmodium falciparum*. *Int J Parasitol* **42**, 529-34 (2012).
37. Su, X.Z. *et al.* A genetic map and recombination parameters of the human malaria parasite *Plasmodium falciparum*. *Science* **286**, 1351-1353 (1999).
38. Amambua-Ngwa, A. *et al.* Chloroquine resistance evolution in *Plasmodium falciparum* is mediated by the putative amino acid transporter AAT1. *Nat Microbiol* **8**, 1213-1226 (2023).
39. Amberg-Johnson, K. *et al.* Small molecule inhibition of apicomplexan FtsH1 disrupts plastid biogenesis in human pathogens. *Elife* **6**, e29865 (2017).
40. Cowell, A.N. *et al.* Mapping the malaria parasite druggable genome by using *in vitro* evolution and chemogenomics. *Science* **359**, 191-199 (2018).
41. Goodman, C.D., Uddin, T., Spillman, N.J. & McFadden, G.I. A single point mutation in the *Plasmodium falciparum* FtsH1 metalloprotease confers actinonin resistance. *Elife* **9**, e58629 (2020).
42. Zhang, M. *et al.* Uncovering the essential genes of the human malaria parasite *Plasmodium falciparum* by saturation mutagenesis. *Science* **360**, eaap7847 (2018).
43. The Pf3K Project: pilot data release 3. (2015).
44. Krogh, A., Larsson, B., von Heijne, G. & Sonnhammer, E.L. Predicting transmembrane protein topology with a hidden Markov model: application to complete genomes. *J Mol Biol* **305**, 567-80 (2001).
45. Hoffman, K. & Stoffel, W. TMbase-a database of membrane spanning proteins segments. *Biochim Biophys Acta* **815**, 468-476 (1993).
46. Jumper, J. *et al.* Highly accurate protein structure prediction with AlphaFold. *Nature* **596**, 583-589 (2021).
47. Kim, J. *et al.* Structure and drug resistance of the *Plasmodium falciparum* transporter PfCRT. *Nature* **576**, 315-320 (2019).
48. Liu, W. *et al.* Origin of the human malaria parasite *Plasmodium falciparum* in gorillas. *Nature* **467**, 420-5 (2010).
49. Dziekan, J.M. *et al.* Cellular thermal shift assay for the identification of drug-target interactions in the *Plasmodium falciparum* proteome. *Nat Protoc* **15**, 1881-1921 (2020).
50. Foley, M. & Tilley, L. Quinoline antimalarials: mechanisms of action and resistance and prospects for new agents. *Pharmacol Ther* **79**, 55-87 (1998).
51. Straimer, J. *et al.* Site-specific genome editing in *Plasmodium falciparum* using engineered zinc-finger nucleases. *Nat Methods* **9**, 993-8 (2012).
52. Palacpac, N.M. *et al.* Developmental-stage-specific triacylglycerol biosynthesis, degradation and trafficking as lipid bodies in *Plasmodium falciparum*-infected erythrocytes. *J Cell Sci* **117**, 1469-80 (2004).
53. Jackson, K.E. *et al.* Food vacuole-associated lipid bodies and heterogeneous lipid environments in the malaria parasite, *Plasmodium falciparum*. *Mol Microbiol* **54**, 109-22 (2004).

54. Hartwig, C.L. *et al.* Accumulation of artemisinin trioxane derivatives within neutral lipids of *Plasmodium falciparum* malaria parasites is endoperoxide-dependent. *Biochem Pharmacol* **77**, 322-36 (2009).
55. Birnbaum, J. *et al.* A Kelch13-defined endocytosis pathway mediates artemisinin resistance in malaria parasites. *Science* **367**, 51-59 (2020).
56. Gnadig, N.F. *et al.* Insights into the intracellular localization, protein associations and artemisinin resistance properties of *Plasmodium falciparum* K13. *PLoS Pathog* **16**, e1008482 (2020).
57. Yang, T. *et al.* Decreased K13 abundance reduces hemoglobin catabolism and proteotoxic stress, underpinning artemisinin resistance. *Cell Rep* **29**, 2917-2928 e5 (2019).
58. Ecker, A., Lehane, A.M., Clain, J. & Fidock, D.A. PfCRT and its role in antimalarial drug resistance. *Trends Parasitol* **28**, 504-14 (2012).
59. Carter, M.D., Phelan, V.V., Sandlin, R.D., Bachmann, B.O. & Wright, D.W. Lipophilic mediated assays for beta-hematin inhibitors. *Comb Chem High Throughput Screen* **13**, 285-92 (2010).
60. Sandlin, R.D. *et al.* Use of the NP-40 detergent-mediated assay in discovery of inhibitors of beta-hematin crystallization. *Antimicrob Agents Chemother* **55**, 3363-9 (2011).
61. Olafson, K.N., Nguyen, T.Q., Rimer, J.D. & Vekilov, P.G. Antimalarials inhibit hematin crystallization by unique drug-surface site interactions. *Proc Natl Acad Sci USA* **114**, 7531-7536 (2017).
62. Combrinck, J.M. *et al.* Insights into the role of heme in the mechanism of action of antimalarials. *ACS Chem Biol* **8**, 133-7 (2013).
63. Bendrat, K., Berger, B.J. & Cerami, A. Haem polymerization in malaria. *Nature* **378**, 138-9 (1995).
64. Wellems, T.E., Walker-Jonah, A. & Panton, L.J. Genetic mapping of the chloroquine-resistance locus on *Plasmodium falciparum* chromosome 7. *Proc Natl Acad Sci USA* **88**, 3382-6 (1991).
65. Waller, K.L. *et al.* Chloroquine resistance modulated *in vitro* by expression levels of the *Plasmodium falciparum* chloroquine resistance transporter. *J Biol Chem* **278**, 33593-601 (2003).
66. Sanchez, C.P. *et al.* The knock-down of the chloroquine resistance transporter PfCRT is linked to oligopeptide handling in *Plasmodium falciparum*. *Microbiol Spectr* **10**, e0110122 (2022).
67. Tanveer, A. *et al.* An FtsH protease is recruited to the mitochondrion of *Plasmodium falciparum*. *PLoS One* **8**, e74408 (2013).
68. Dahl, E.L. & Rosenthal, P.J. Multiple antibiotics exert delayed effects against the *Plasmodium falciparum* apicoplast. *Antimicrob Agents Chemother* **51**, 3485-90 (2007).
69. Lewis, I.A. *et al.* Metabolic QTL analysis links chloroquine resistance in *Plasmodium falciparum* to impaired hemoglobin catabolism. *PLoS Genet* **10**, e1004085 (2014).
70. Shafik, S.H. *et al.* The natural function of the malaria parasite's chloroquine resistance transporter. *Nat Commun* **11**, 3922 (2020).

71. Okombo, J. *et al.* Piperaquine-resistant PfCRT mutations differentially impact drug transport, hemoglobin catabolism and parasite physiology in *Plasmodium falciparum* asexual blood stages. *PLoS Pathog* **18**, e1010926 (2022).
72. Howe, R., Kelly, M., Jimah, J., Hodge, D. & Odom, A.R. Isoprenoid biosynthesis inhibition disrupts Rab5 localization and food vacuolar integrity in *Plasmodium falciparum*. *Eukaryot Cell* **12**, 215-23 (2013).
73. Kennedy, K. *et al.* Delayed death in the malaria parasite *Plasmodium falciparum* is caused by disruption of prenylation-dependent intracellular trafficking. *PLoS Biol* **17**, e3000376 (2019).
74. Vaughan, A.M. *et al. Plasmodium falciparum* genetic crosses in a humanized mouse model. *Nat Methods* **12**, 631-3 (2015).
75. Azuma, H. *et al.* Robust expansion of human hepatocytes in *Fah*$^{-/-}$/*Rag2*$^{-/-}$/*Il2rg*$^{-/-}$ mice. *Nat Biotechnol* **25**, 903-10 (2007).
76. Li, H. & Durbin, R. Fast and accurate short read alignment with Burrows-Wheeler transform. *Bioinformatics* **25**, 1754-60 (2009).
77. Cingolani, P. *et al.* A program for annotating and predicting the effects of single nucleotide polymorphisms, SnpEff: SNPs in the genome of *Drosophila melanogaster* strain *w*^{1118}; *iso-2*; *iso-3*. *Fly* **6**, 80-92 (2012).
78. Kanai, M. *et al.* Comparative analysis of *Plasmodium falciparum* genotyping via SNP detection, microsatellite profiling, and whole-genome sequencing. *Antimicrob Agents Chemother* **66**, e0116321 (2022).
79. Li, H. *et al.* The sequence alignment/map format and SAMtools. *Bioinformatics* **25**, 2078-2079 (2009).
80. de Hoon, M.J., Imoto, S., Nolan, J. & Miyano, S. Open source clustering software. *Bioinformatics* **20**, 1453-1454 (2004).
81. Saldanha, A.J. Java Treeview--extensible visualization of microarray data. *Bioinformatics* **20**, 3246-3248 (2004).
82. Mansfeld, B.N. & Grumet, R. QTLseqr: an R package for bulk segregant analysis with next-generation sequencing. *Plant Genome* **11** (2018).
83. Takagi, H. *et al.* QTL-seq: rapid mapping of quantitative trait loci in rice by whole genome resequencing of DNA from two bulked populations. *Plant J* **74**, 174-83 (2013).
84. Magwene, P.M., Willis, J.H. & Kelly, J.K. The statistics of bulk segregant analysis using next generation sequencing. *PLoS Comput Biol* **7**, e1002255 (2011).
85. Broman, K.W., Wu, H., Sen, S. & Churchill, G.A. R/qtl: QTL mapping in experimental crosses. *Bioinformatics* **19**, 889-90 (2003).
86. Adjalley, S. & Lee, M.C.S. CRISPR/Cas9 editing of the *Plasmodium falciparum* genome. *Methods Mol Biol* **2470**, 221-239 (2022).
87. Labun, K. *et al.* CHOPCHOP v3: expanding the CRISPR web toolbox beyond genome editing. *Nucleic Acids Res* **47**, W171-W174 (2019).
88. Roy, K.R. *et al.* Multiplexed precision genome editing with trackable genomic barcodes in yeast. *Nat Biotechnol* **36**, 512-520 (2018).
89. Fidock, D.A., Nomura, T. & Wellems, T.E. Cycloguanil and its parent compound proguanil demonstrate distinct activities against *Plasmodium falciparum* malaria parasites transformed with human dihydrofolate reductase. *Mol Pharmacol* **54**, 1140-7 (1998).

90. Adjalley, S.H., Lee, M.C. & Fidock, D.A. A method for rapid genetic integration into *Plasmodium falciparum* utilizing mycobacteriophage Bxb1 integrase. *Methods Mol Biol* **634**, 87-100 (2010).
91. Fidock, D.A. & Wellems, T.E. Transformation with human *dihydrofolate reductase* renders malaria parasites insensitive to WR99210 but does not affect the intrinsic activity of proguanil. *Proc Natl Acad Sci USA* **94**, 10931-6 (1997).
92. Murithi, J.M. *et al.* The *Plasmodium falciparum* ABC transporter ABCI3 confers parasite strain-dependent pleiotropic antimalarial drug resistance. *Cell Chem Biol* **29**, 824-839 e6 (2022).
93. Schindelin, J. *et al.* Fiji: an open-source platform for biological-image analysis. *Nat Methods* **9**, 676-82 (2012).
94. Amos, B. *et al.* VEuPathDB: the eukaryotic pathogen, vector and host bioinformatics resource center. *Nucleic Acids Res* **50**, D898-D911 (2022).
95. Sievers, F. *et al.* Fast, scalable generation of high-quality protein multiple sequence alignments using Clustal Omega. *Mol Syst Biol* **7**, 539 (2011).
96. Needleman, S.B. & Wunsch, C.D. A general method applicable to the search for similarities in the amino acid sequence of two proteins. *J Mol Biol* **48**, 443-53 (1970).
97. Madeira, F. *et al.* Search and sequence analysis tools services from EMBL-EBI in 2022. *Nucleic Acids Res* **50**, W276-W279 (2022).
98. Goehring, A. *et al.* Screening and large-scale expression of membrane proteins in mammalian cells for structural studies. *Nat Protoc* **9**, 2574-85 (2014).
99. Ncokazi, K.K. & Egan, T.J. A colorimetric high-throughput beta-hematin inhibition screening assay for use in the search for antimalarial compounds. *Anal Biochem* **338**, 306-19 (2005).
100. Lopez-Barragan, M.J. *et al.* Directional gene expression and antisense transcripts in sexual and asexual stages of *Plasmodium falciparum*. *BMC Genomics* **12**, 587 (2011).
101. Bushell, E. *et al.* Functional profiling of a *Plasmodium* genome reveals an abundance of essential genes. *Cell* **170**, 260-272 (2017).

Figure 1

a NF54 × Cam3.II genetic cross parents

Genetic Cross Parents	Geographical Origin (Year Adapted to Culture)	*pfmdr1* Chr 5		*pfcrt* Chr 7	*k13* Chr 13	*pm2/3* Chr 14	Resistance Phenotype (Geometric mean IC_{50} in nM) CQ	md-CQ	QN	md-ADQ	MFQ	LMF
NF54	Africa (1979)	WT	1 copy	WT	WT	1 copy	S (9.0)	S (21.6)	S (14.2)	S^{hi} (6.9)	S^{hi} (6.6)	S^{hi} (3.6)
Cam3.II	Pursat, (W.) Cambodia (2010)	Y184F	2 copies	Dd2[a]	R539T	1 copy	R (83.2)	R (947.7)	R^{mod} (117.6)	S^{lo} (28.2)	S^{lo} (11.8)	S^{lo} (4.1)

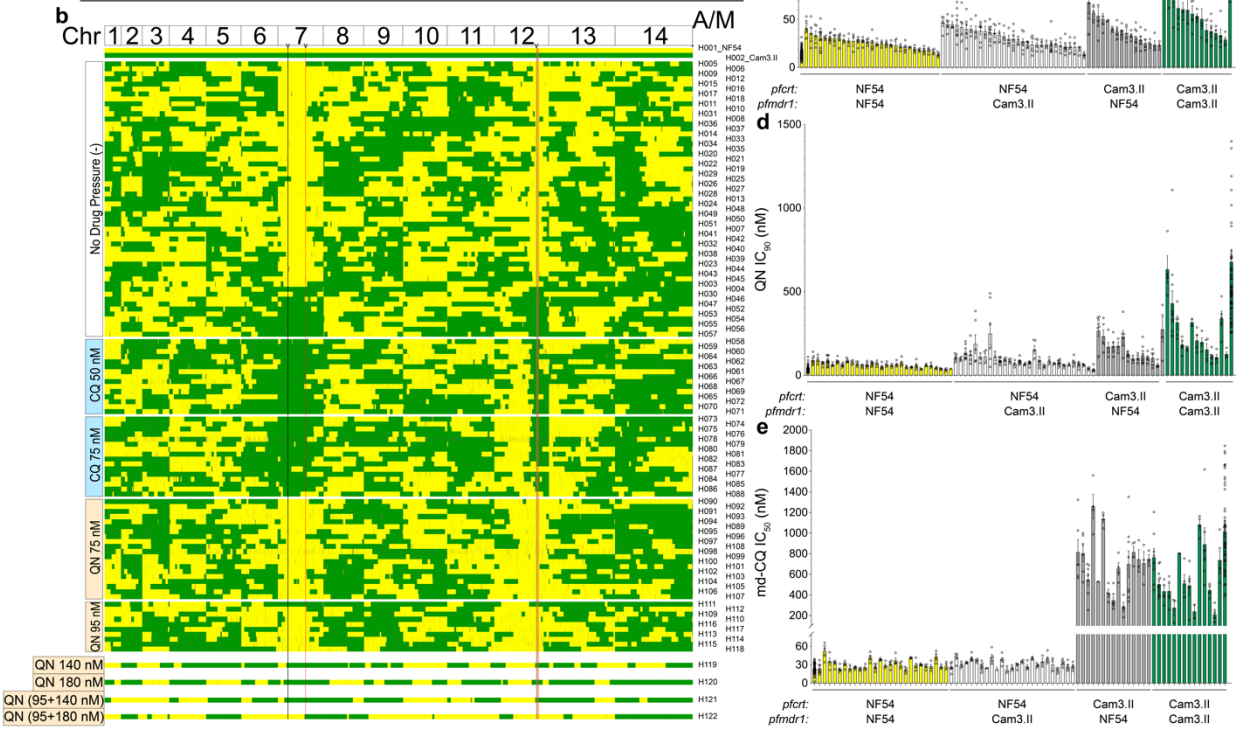

Fig. 1 | A *P. falciparum* NF54×Cam3.II genetic cross yielded 120 independent recombinant progeny with diverse genomic and drug resistance profiles. a, NF54×Cam3.II genetic cross parent information. [a]Dd2 PfCRT haplotype: M74I/N75E/K76T/A220S/Q271E/N326S/I356T/R371I. *k13*: kelch13 (PF3D7_1343700); *pfcrt*: chloroquine resistance transporter (PF3D7_0709000); *pfmdr1*: multidrug resistance protein 1 (PF3D7_0523000). ADQ: amodiaquine; ART: artemisinin; CQ: chloroquine; LMF: lumefantrine; md-ADQ: mono-desethyl amodiaquine; md-CQ: monodesethyl-chloroquine; MFQ: mefloquine; md-CQ: monodesethyl-chloroquine; PPQ: piperaquine; QN: quinine. R, resistant; R^{mod}, moderate resistance; S, sensitive; S^{hi}, high sensitivity; S^{lo}, low sensitivity. Geometric mean IC_{50} values in nM are listed in the parentheses (N=4–85 with technical duplicates). **b**, Recombinant progeny representing each of 120 unique haplotypes were hierarchically clustered by similarity based on their NF54 (yellow) or Cam3.II (green) alleles at 13,116 SNP positions within each selection condition: no drug pressure, chloroquine (CQ) 50 nM or 75 nM, or quinine (QN) 75 nM, 95 nM, 140 nM, 180 nM, (95nM+140nM), (95nM+180nM), or (95nM+140nM+240nM), in that order. Some haplotypes were obtained in more than one selection condition (**Table S4**). NF54 (H001) and Cam3.II (H002) parents are shown on top. H, haplotype; A/M, apicoplast/mitochondria (these were always coinherited); black line, *pfcrt*; red line, *dmt1;* grey line*, ftsh1*; red box, QN IC_{90}, md-CQ IC_{90}, CQ IC_{50} and IC_{90} chromosome 12 QTL locus. **c-e**, Mean ± SEM QN IC_{50} and IC_{90} values are shown in **c** and **d**, respectively, and md-CQ IC_{50} values are shown in **e** (N,n=1–85, with a majority of >4, with technical duplicates). Data were generated with parasites cultured in media with Albumax (no serum).

Figure 2

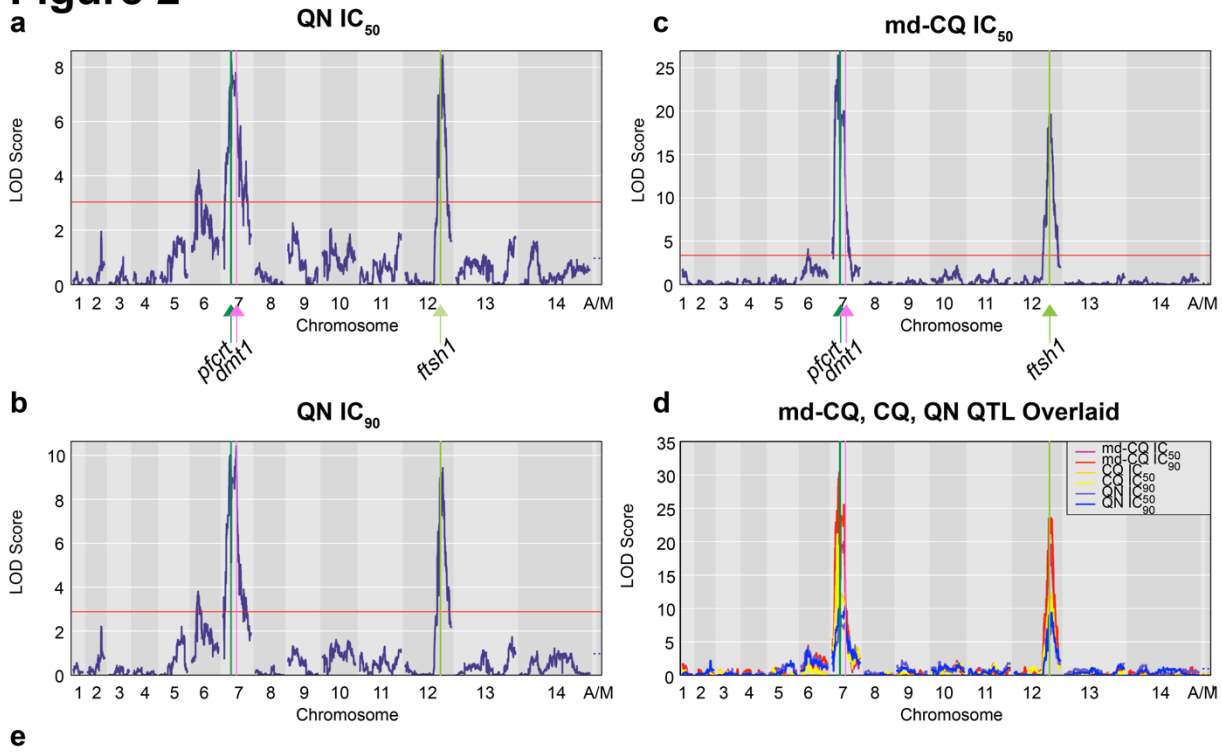

e

List of significant QTL segments identified by progeny clone-based analyses.

Drug response phenotypes	Chromosome	Position	LOD Score	Start position	End position	Size (bp)	% variance	Genes of interest
QN IC_{50}	6	387,269	4.21	242,806	967,817	725,011	19.0%	
QN IC_{50}	7	468,471	8.25	392,420	719,023	326,603	33.8%	*dmt1 + pfcrt*
QN IC_{50}	12	1,780,135	8.43	1,564,694	1,846,858	282,164	34.4%	*thzk + ftsh1 + samc*
QN IC_{90}	6	362,644	3.80	255,008	967,817	712,809	18.2%	
QN IC_{90}	7	701,206	10.42	379,842	717,936	338,094	42.4%	*dmt1 + pfcrt*
QN IC_{90}	12	1,780,135	9.43	1,644,803	1,791,218	146,415	39.3%	*thzk + ftsh1 + samc*
md-CQ IC_{50}	6	404,679	4.12	242,806	1,163,974	921,168	20.6%	
md-CQ IC_{50}	7	369,222	26.41	369,222	434,294	65,072	77.3%	*pfcrt*
md-CQ IC_{50}	12	1,746,445	19.60	1,666,819	1,749,151	82,332	66.7%	
md-CQ IC_{90}	6	404,679	4.50	281,586	1,211,193	929,607	23.0%	
md-CQ IC_{90}	7	414,358	30.40	383,125	435,497	52,372	83.0%	*pfcrt*
md-CQ IC_{90}	12	1,732,975	23.58	1,644,803	1,791,218	146,415	74.7%	*thzk + ftsh1 + samc*
CQ IC_{50}	7	414,358	19.10	379,842	433,609	53,767	81.6%	*pfcrt*
CQ IC_{50}	12	1,770,830	12.16	1,644,803	1,791,218	146,415	66.0%	*thzk + ftsh1 + samc*
CQ IC_{90}	7	342,797	21.17	313,716	373,413	59,697	84.7%	
CQ IC_{90}	12	1,770,830	11.27	1,644,803	1,791,218	146,415	63.2%	*thzk + ftsh1 + samc*

Fig. 2 | QTL mapping of QN, CQ, and md-CQ progeny reveals a non-*pfcrt*-centered chromosome 7 QN IC_{90} peak and an additional shared peak on chromosome 12.
a-c, LOD plots for mean QN IC_{50} (**a**), QN IC_{90} (**b**), and md-CQ IC_{50} (**c**) values. The red line indicates the 95% probability threshold. **d**, md-CQ, CQ, and QN LOD plots overlaid. QTL, quantitative trait locus; LOD, log of the odds; md-CQ, monodesethyl-chloroquine; CQ, chloroquine; QN, quinine; IC_{50} and IC_{90}, 50% and 90% growth inhibitory concentrations. **e**, List of significant QTL segments identified by progeny clone-based analysis. chromosome 7: *pfcrt* (dark green line), *dmt1* (pink line). chromosome 12: *thzk* and *ftsh1* (light green line).

Figure 3

a Top candidate genes from progeny clone-based QN, CQ, and md-CQ QTL analyses.

QTL	Gene Name	Gene Location	SNPs between NF54, Cam3.II	Mutable in *P. falciparum* CDS[b]	*P. falciparum* mutant fitness	*P. berghei* KO (PlasmoGEM)[c]	Association with antiplasmodial resistance
QN chr 7 IC_{50}	chloroquine resistance transporter (*pfcrt*)	Pf3D7_07_v3:402,385..406,341	Dd2[a]	No	-3.03	Essential	CQ
QN chr 7 IC_{50} and IC_{90}	drug metabolite transporter 1 (*dmt1*), putative	Pf3D7_07_v3:695,091..697,180	Y107N/S129L/N155	Yes	-3.05	Dispensable	QN (this paper)
QN, CQ, md-CQ chr 12	hydroxyethylthiazole kinase (*thzk*)	Pf3D7_12_v3:1,652,687..1,654,402	N244/A301V	Yes	-2.16	N/A	Putative MMV inhibitor target[d]
	ATP-dependent zinc metalloprotease (*ftsh1*)	Pf3D7_12_v3:1,654,438..1,658,821	D695G	Yes	-1.02	ND	G489C confers actinonin resistance[e]
	S-adenosylmethionine mitochondrial carrier protein (*samc*), putative	Pf3D7_12_v3:1,774,021..1,776,962	I176K/S193A	No	-3.31	Essential	MMV019662, MMV028038 selected for CNVs[f]

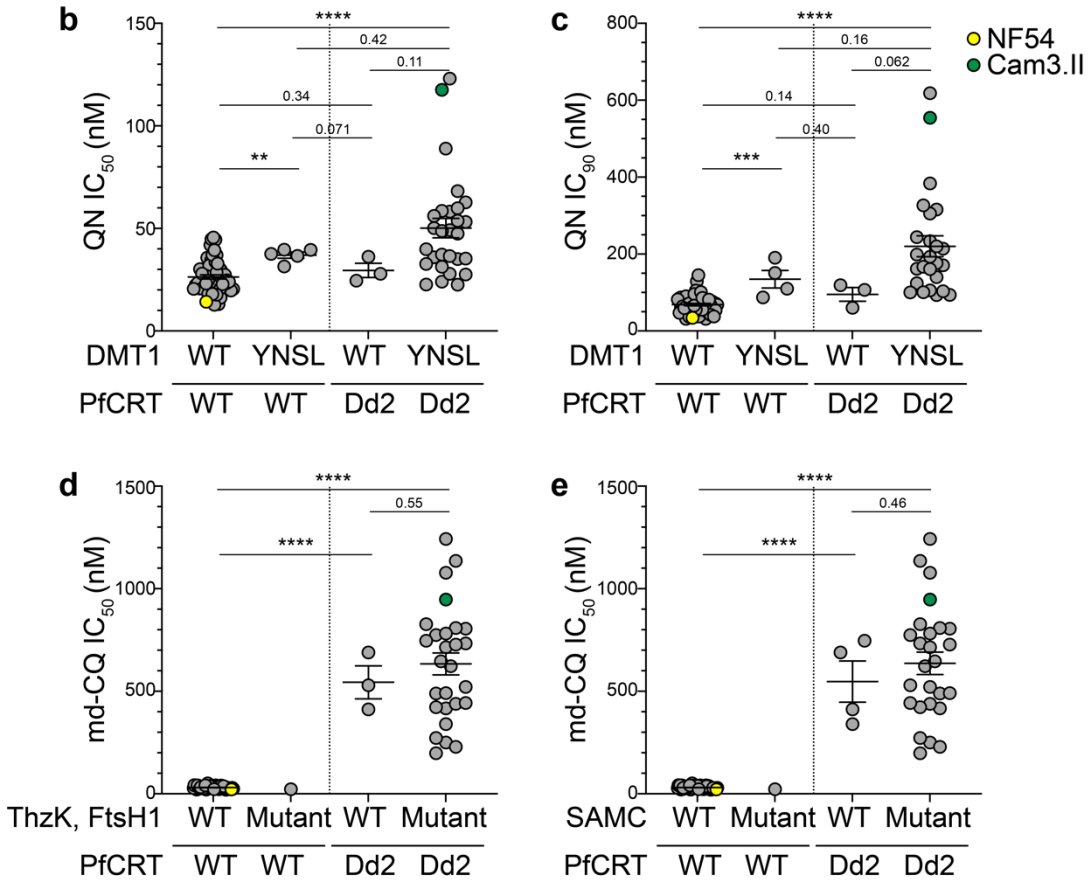

Fig. 3 | Identification of the top candidate genes from the QN chromosome 7 and QN, CQ, md-CQ chromosome 12 QTL peaks.

a, Top candidate genes from progeny clone-based QN, CQ, and md-CQ QTL analyses. All genes are expressed in the *P. falciparum* ABS parasites[100]. QTL, quantitative trait locus; SNP, single-nucleotide polymorphism; QN, quinine; CQ, chloroquine; md, monodesethyl; CDS, coding sequence; KO, knockout; CNV, copy number variants; ND, not determined; N/A, not applicable. [a]Dd2 PfCRT haplotype: M74I/N75E/K76T/A220S/Q271E/N326S/I356T/R371I. [b]ref. 42, the closer the mutant fitness score is to -4, the higher the predicted fitness cost. [c]ref. 101. [d]Personal communication with Dr. Susan Wyllie. [e]ref. 41. [f]ref. 40. **b**-**e**, QN (**b**,**c**) and md-CQ. **d**,**e**, IC levels for the profiled unedited cross progeny and two parents, grouped by *pfcrt*, *dmt1*, *thzk*, *ftsh1*, and *samc* genotypes. Statistical significance was determined by Mann-Whitney *U* tests (N,n=1–27, with technical duplicates). $^{**}p < 0.01$, $^{***}p < 0.001$, $^{***}p < 0.0001$.

Figure 4

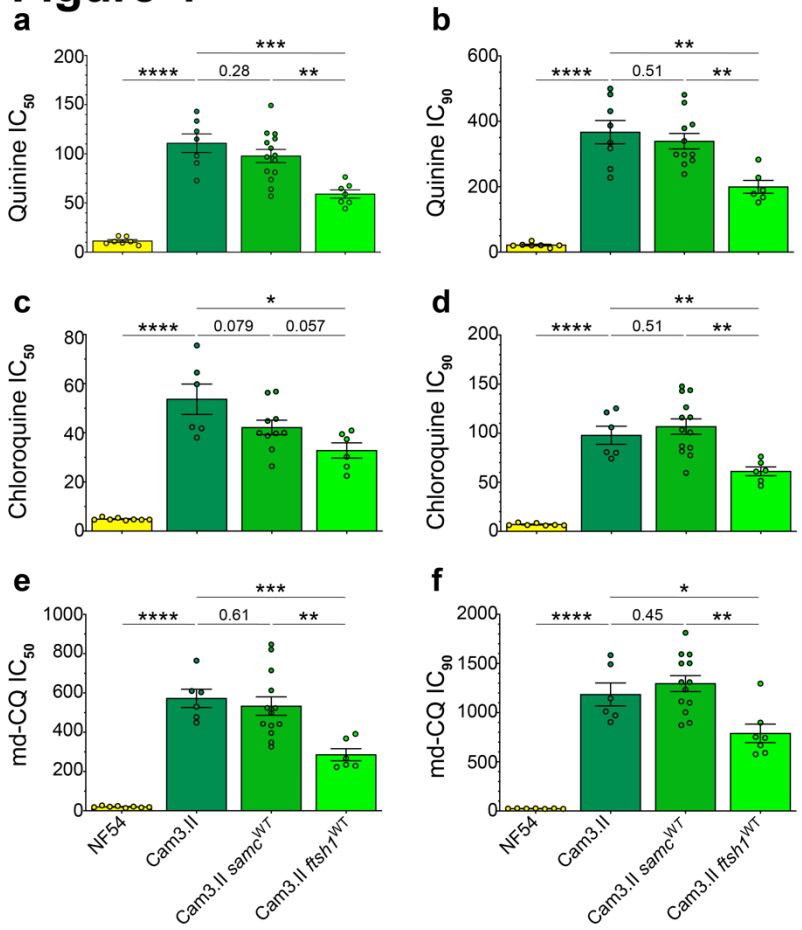

Fig. 4 | *ftsh1* is a candidate gene for the chromosome 12 QTL locus.
a-**f**, Quinine (**a**,**b**), chloroquine (**c**,**d**), and md-Chloroquine (**e**,**f**) response in *samc* and *ftsh1* SNP-edited Cam3.II as measured by mean ± SEM IC_{50} or IC_{90} values. For each parasite, the parental unedited parasite (endogenous haplotype) (dark color) and the SNP-edited parasite (wild-type revertant parasite) (light color) were profiled. *p*-values (Student's *t*-test) are indicated (N,n=6–16,2). *$p < 0.05$; **$p < 0.01$; ***$p < 0.001$.

Figure 5

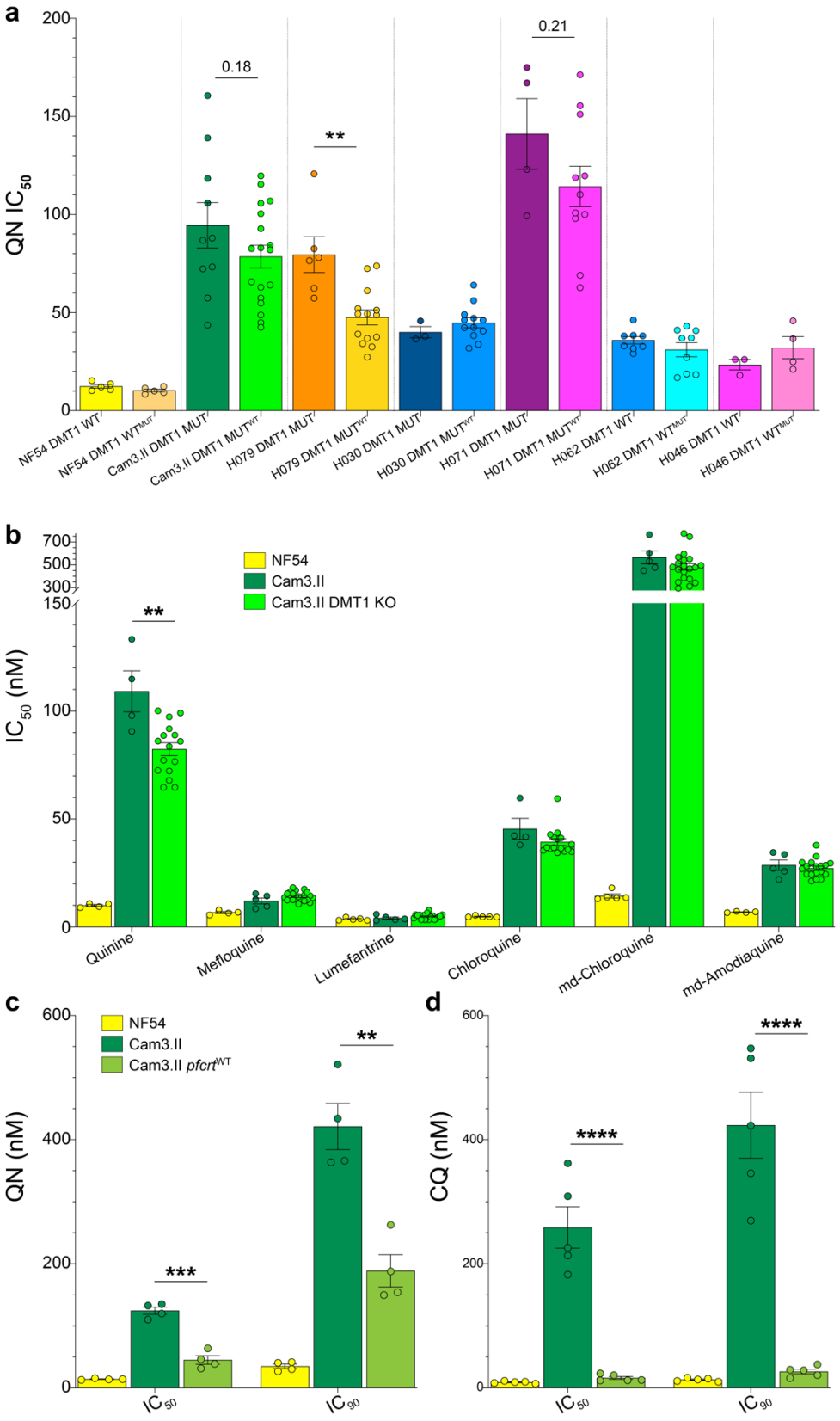
a
QN IC50
0.18
**
0.21
NF54 DMT1 WT/
NF54 DMT1 WTMUT/
Cam3.II DMT1 MUT/
Cam3.II DMT1 MUTWT/
H079 DMT1 MUT/
H079 DMT1 MUTWT/
H030 DMT1 MUT/
H030 DMT1 MUTWT/
H071 DMT1 MUT/
H071 DMT1 MUTWT/
H062 DMT1 WT/
H062 DMT1 WTMUT/
H046 DMT1 WT/
H046 DMT1 WTMUT/
b
IC50 (nM)
NF54
Cam3.II
Cam3.II DMT1 KO
**
Quinine
Mefloquine
Lumefantrine
Chloroquine
md-Chloroquine
md-Amodiaquine
c
QN (nM)
NF54
Cam3.II
Cam3.II pfcrtWT
***
**
IC50
IC90
d
CQ (nM)
****
****
IC50
IC90

Fig. 5 | Cam3.II parasites lacking DMT1 or expressing WT PfCRT are significantly sensitized to QN.

a, Quinine response of DMT1 SNP-edited parents and progeny as measured by mean ± SEM IC_{50} values. For each parasite, the parental unedited parasite (endogenous DMT1 haplotype) and the SNP-edited parasite (Y107N / S129L mutant or wild-type revertant haplotype) are indicated by dark and light colors, respectively. *p* values (Student's *t*-test) are indicated (N,n=2–8,2). WT, wild-type; YNSL, Y107N / S129L mutation. **b**, Quinine, mefloquine, lumefantrine, chloroquine, md-Chloroquine, md-Amodiaquine response in Cam3.II DMT1 knockout parasites as measured by mean ± SEM IC_{50} values. *p*-values (Student's *t*-test) are indicated for the Cam3.II KO strain vs the Cam3.II parent (N=4–21, with technical duplicates). **c-d**, Quinine (**c**) and chloroquine (**d**) response in Cam3.II *pfcrt*^{WT} revertant parasites as measured by mean ± SEM IC_{50} and IC_{90} values. *p*-values (Student's *t*-test) are indicated for the Cam3.II *pfcrt*^{WT} strain vs the Cam3.II parent (N=4–5, with technical duplicates). *$p < 0.05$; **$p < 0.01$; ***$p < 0.001$; ****$p < 0.0001$.

Figure 6

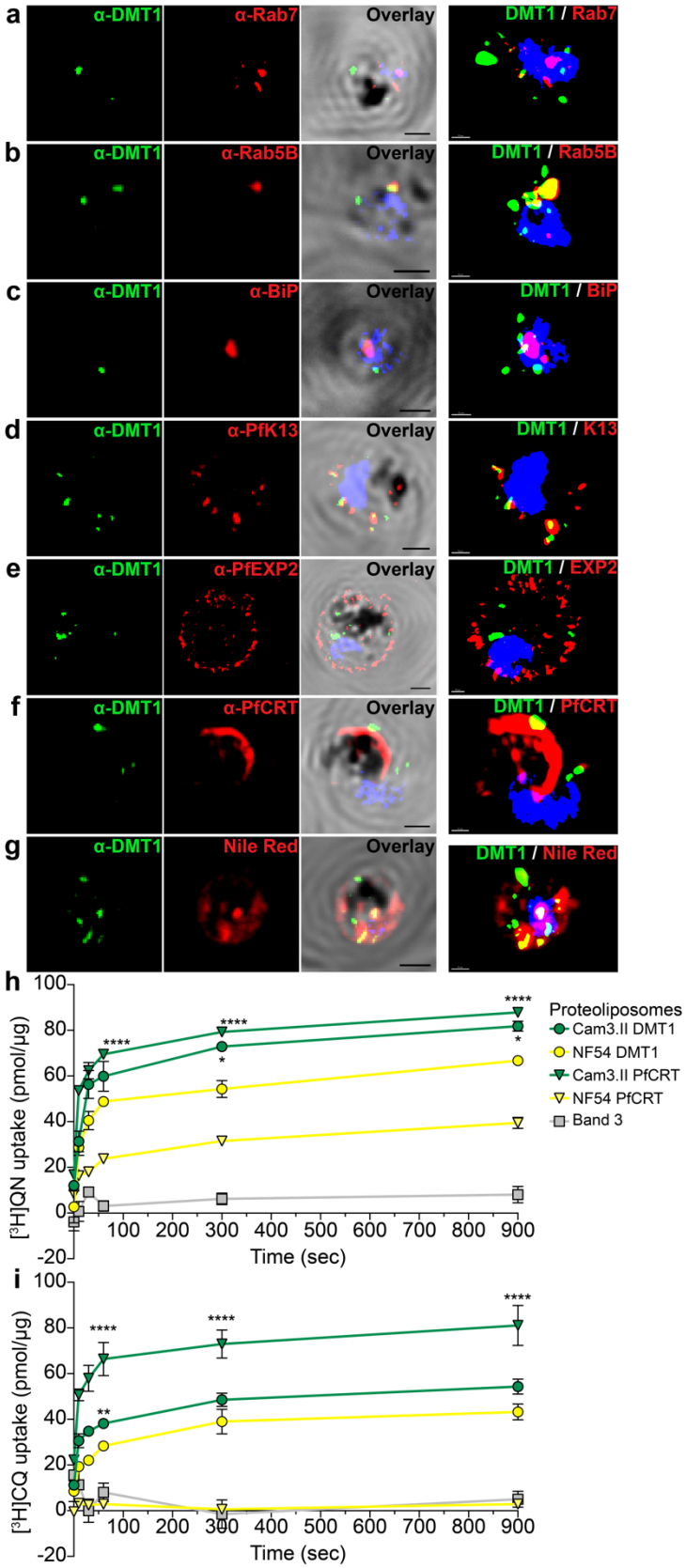
a
α-DMT1
α-Rab7
Overlay
DMT1 / Rab7
b
α-DMT1
α-Rab5B
Overlay
DMT1 / Rab5B
c
α-DMT1
α-BiP
Overlay
DMT1 / BiP
d
α-DMT1
α-PfK13
Overlay
DMT1 / K13
e
α-DMT1
α-PfEXP2
Overlay
DMT1 / EXP2
f
α-DMT1
α-PfCRT
Overlay
DMT1 / PfCRT
g
α-DMT1
Nile Red
Overlay
DMT1 / Nile Red
h
[3H]QN uptake (pmol/µg)
Time (sec)
Proteoliposomes
Cam3.II DMT1
NF54 DMT1
Cam3.II PfCRT
NF54 PfCRT
Band 3
i
[3H]CQ uptake (pmol/µg)
Time (sec)

Fig. 6 | DMT1 shows localization to structures associated with vesicular trafficking as well as the digestive vacuole and exhibits differential uptake of [^{3}H]QN between the NF54 and Cam3.II isoforms.

a-**g**, Representative immunofluorescence assays (IFA) showing DMT1-3×HA-tagged parasites stained with antibodies or dyes: α-HA (DMT1, green), DAPI (nuclear, blue). **a**, α-Rab7 (late endosome), **b**, α-Rab5B (early endosome), **c**, α-BiP (ER), **d**, α-PfK13 (ER, vesicles, near cytostome), **e**, α-PfEXP2 (parasitophorous vacuolar membrane), **f**, α-PfCRT (digestive vacuole membrane), or **g**, Nile Red (lipid bodies). IFA images are shown as 3D volume reconstructions. Scale bars: 1 μm for IFA (black), 0.5 μm for 3D volume reconstructions (white). **h**,**i**, Time course of 300 nM [^{3}H]QN and 300 nM [^{3}H]CQ uptake measured with PfCRT (NF54 or Cam3.II), DMT1 (NF54 or Cam3.II), or Band 3-containing proteoliposomes. Data are mean ± SEM of $n = 3$ independent experiments with technical duplicates. Statistical significance between NF54 and Cam3.II variants for each protein was determined by unpaired Student's *t*-tests corrected for multiple testing (**h**, **i**). *$p < 0.05$, **$p < 0.01$, ****$p < 0.0001$.

Extended Data 1

a

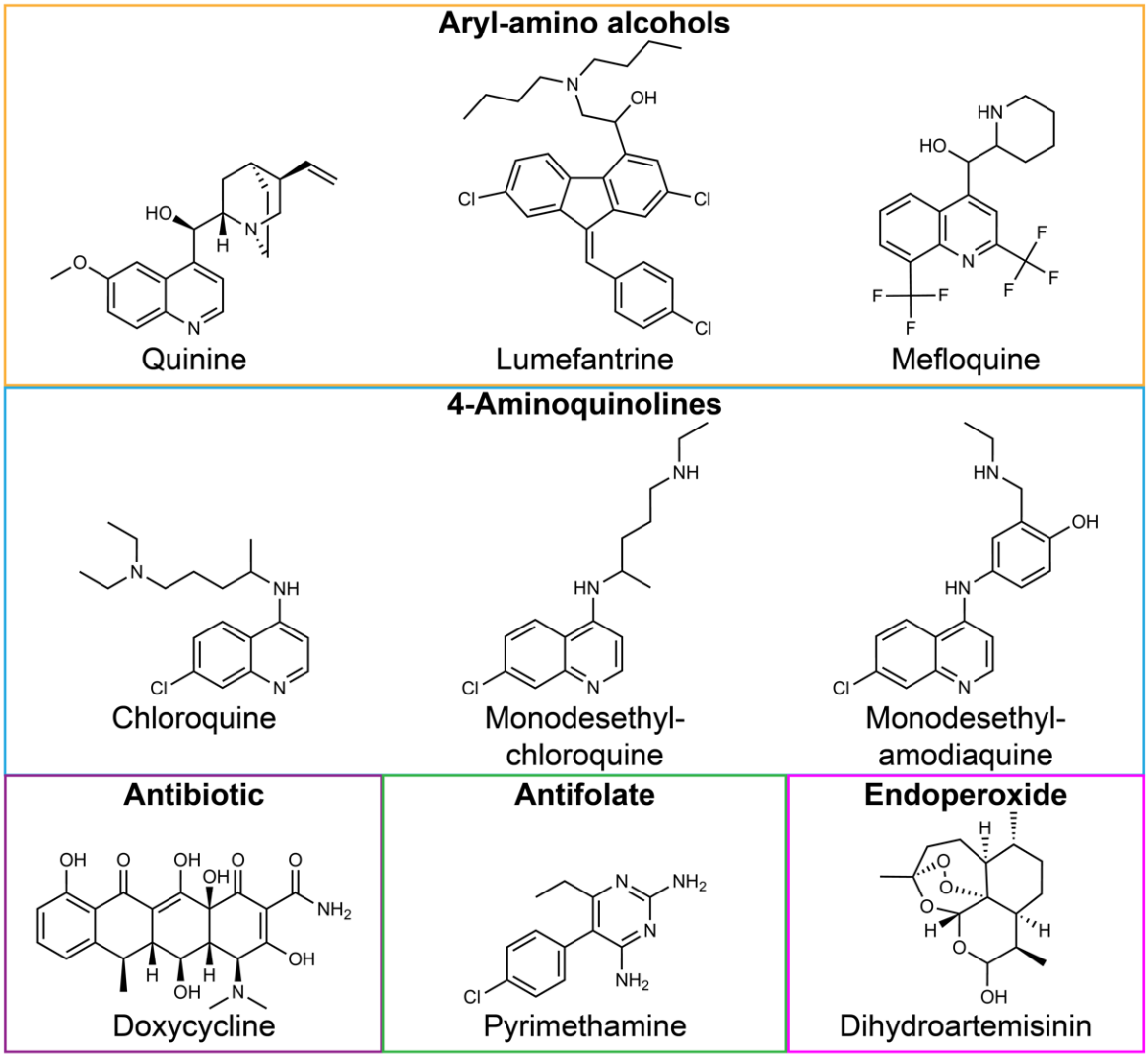

b

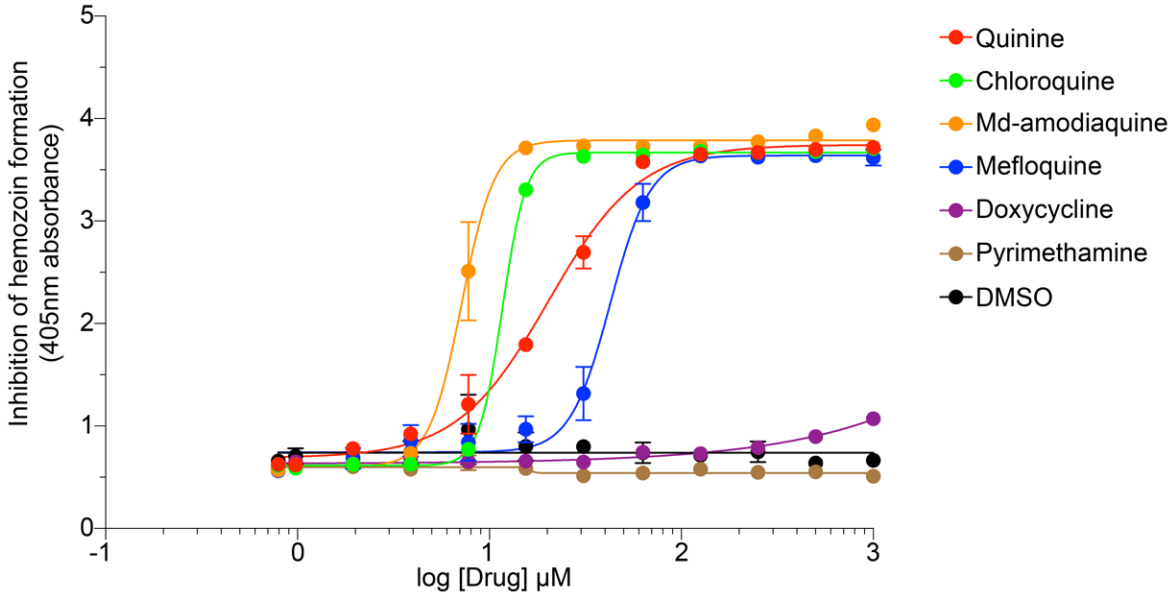

Extended Data 1 | Quinine inhibits β-hematin formation to a lesser degree than chloroquine but more than mefloquine in a cell-free system.

a, Chemical structures of the antiplasmodial compounds used in this study. Quinine, lumefantrine, and mefloquine are aryl-amino alcohols; chloroquine, monodesethyl-chloroquine, and monodesethyl-amodiaquine are 4-aminoquinolines; doxycycline is a tetracycline-class antibiotic; pyrimethamine is an antifolate; dihydroartemisinin is an active metabolite of artemisinin, a sesquiterpene lactone endoperoxide. Quinine and mefloquine have the aminoquinoline ring found in chloroquine, monodesethyl-chloroquine, and monodesethyl-amodiaquine. Chemical formulas, SMILES, and Tanimoto scores of these compounds are indicated in **Table S13**. **b**, Representative concentration-dependent inhibition of β-hematin formation by quinine, chloroquine, md-amodiaquine, mefloquine, two non-heme detoxification pathway-acting negative control antimalarials (doxycycline and pyrimethamine), and DMSO. Mean ± SEM IC_{50} values from N=3 experiments are listed in **Table S12**.

Extended Data Figure 2

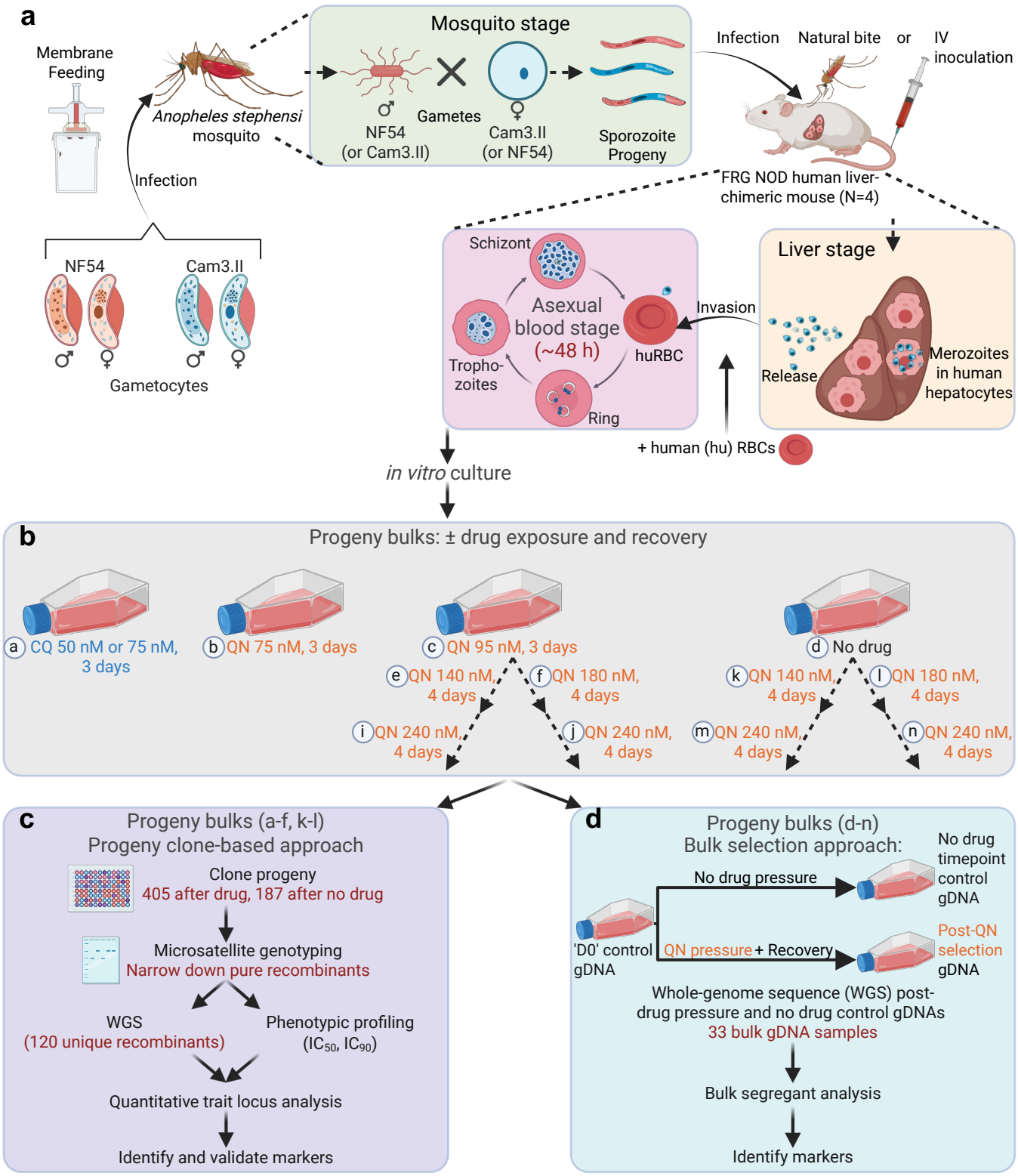

Extended Data 2 | Workflow of the NF54×Cam3.II genetic cross, isolation of progeny, and bulk selection vs. progeny clone-based trait mapping.

a, Overview of the genetic cross performed using *Anopheles stephensi* mosquitoes and FRG NOD human-liver chimeric mice (N=4). RBCs, red blood cells. **b**, Drug selection conditions were applied to progeny bulks, followed by a drug-free recovery period after which bulk genomic DNA was harvested and/or the progeny were cloned out. **c**,**d**, Genetic determinants of drug resistance were identified using progeny clone-based linkage approaches (**c**) or bulk selection approaches with bulk segregant analysis (**d**). Images were created with BioRender.com. The NF54 and Cam3.II parents are described in **Fig. 1a**, the mosquito and mouse infections are described in **Table S1**, and the total number of clonal progeny obtained are indicated in **Table S15**.

Extended Data 3

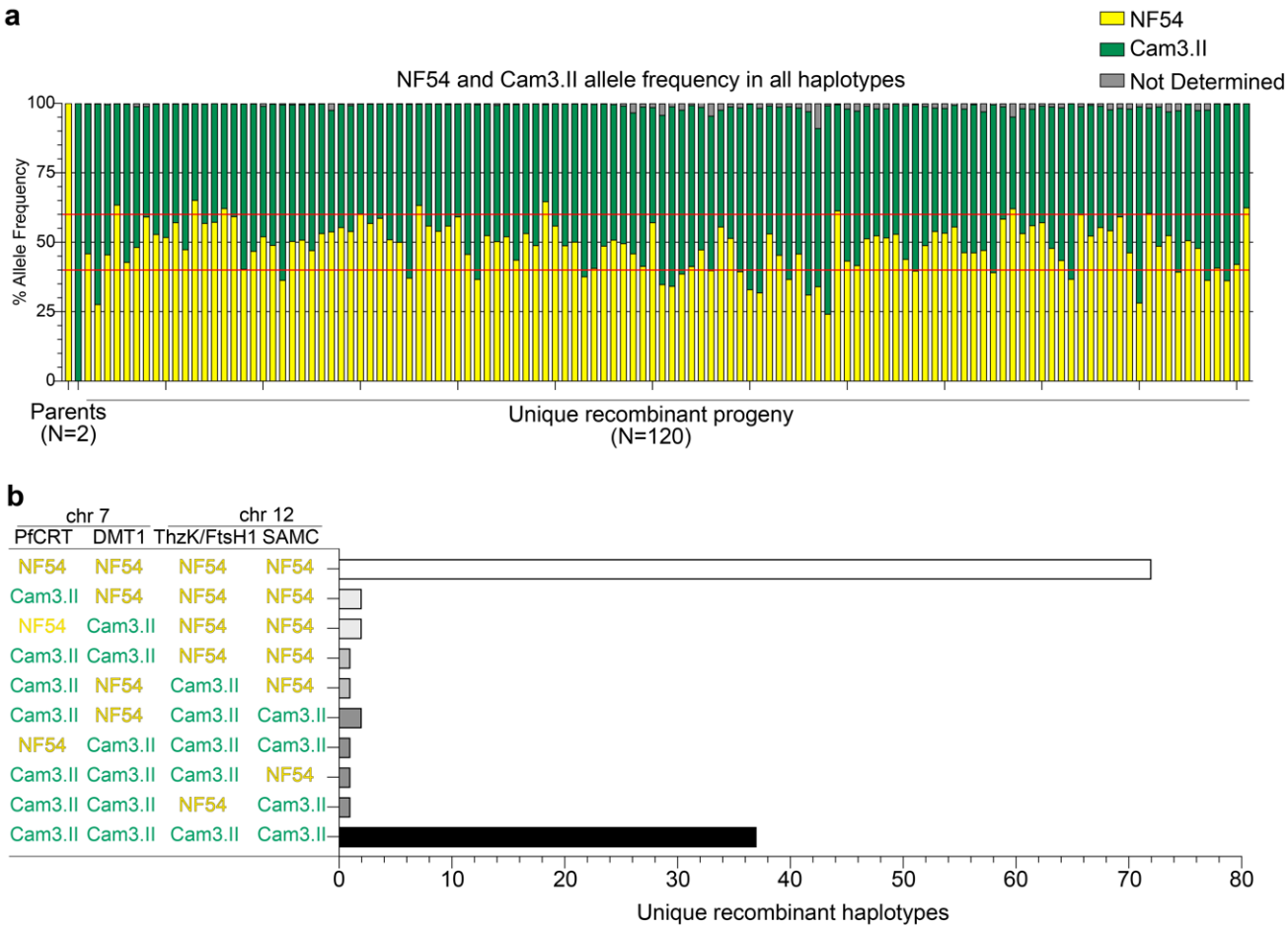

Extended Data 3 | Genome-wide frequencies and *pfcrt*, *dmt1*, *thzk*/*ftsh1*, and *samc* allele representation in the recombinant progeny

a, Percentage of NF54 and Cam3.II allele frequencies averaged across the genome in 13,116 SNP positions for each of the parents and 120 recombinant progeny, ordered by haplotype number. **b**, Number of unique recombinant progeny with the wild-type NF54 or mutant Cam3.II alleles for *pfcrt, dmt1, thzk/ftsh1, and samc.* The mutant Cam3.II alleles for each gene are listed in **Fig. 3a**.

Extended Data 4

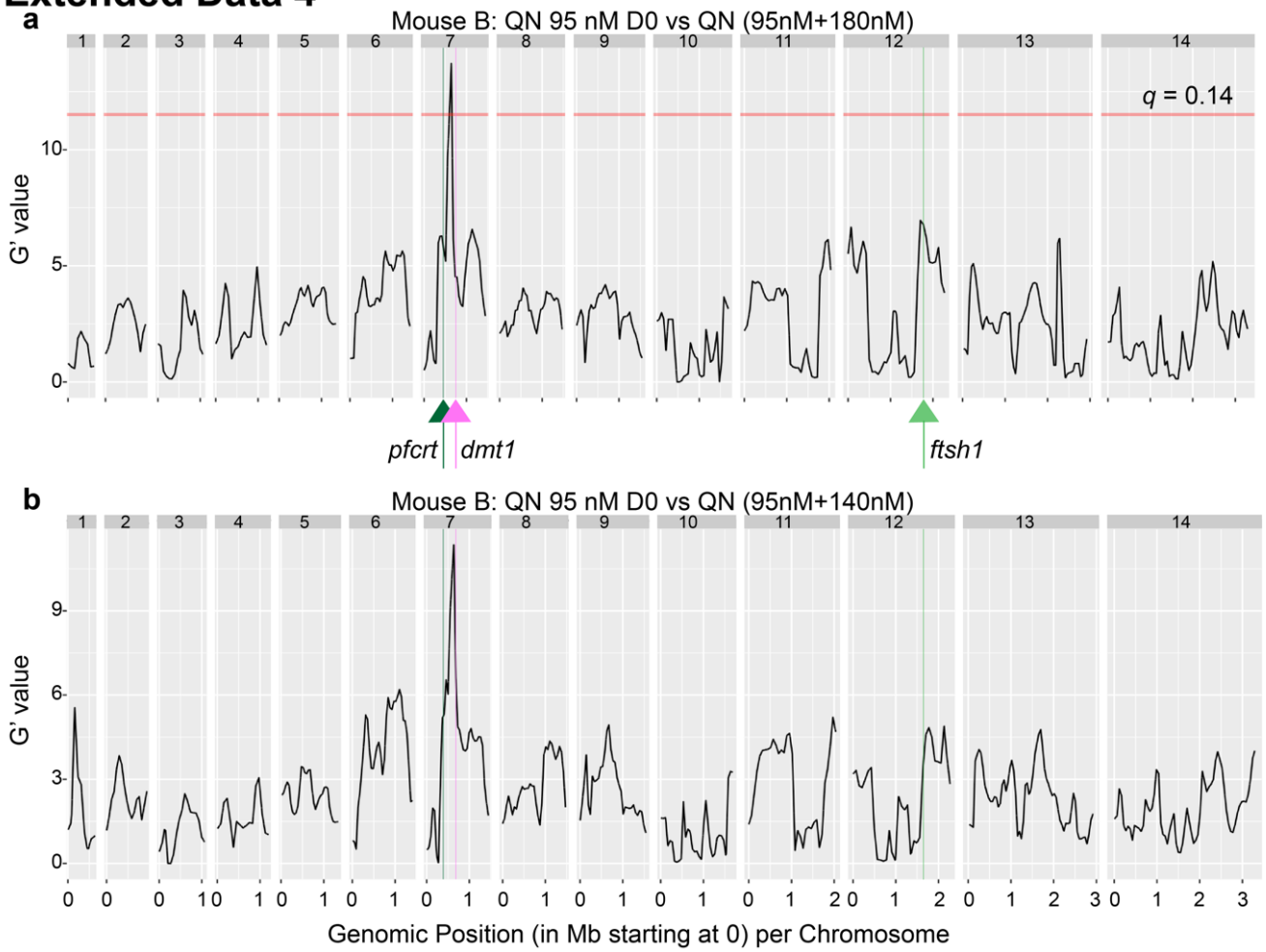

Extended Data 4 | Bulk segregant analyses of progeny pools pressured with quinine or no-drug controls.

a,**b**, Genetic loci enriched by quinine (QN) in drug-no drug pairwise comparisons. Black lines are G' values comparing allele frequency between QN-pressured bulk progeny and control non-drug-pressured bulk progeny. The red line indicates the False Discovery Rate at the indicated threshold. Samples are described in **Table S5**. Quantitative trait locus regions are described in **Table S6**. Of note, mutant *pfcrt*/mutant *ftsh1, or* WT *pfcrt*/WT *ftsh1,* continued to be co-inherited in the QN-pressured progeny, as was seen in the non-drug-pressured progeny.

Extended Data 5

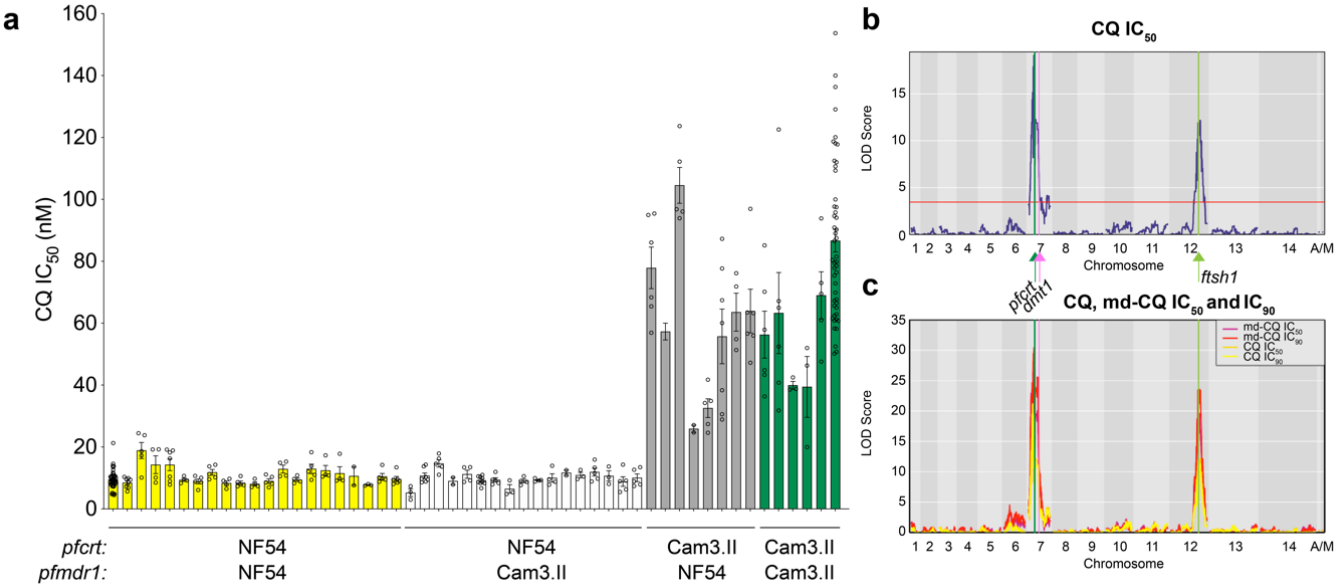

Extended Data 5 | Phenotypic response of parents and recombinant progeny to chloroquine and monodesethyl-chloroquine closely align.
a, Chloroquine (CQ) response as measured by mean ± SEM IC_{50} values. **b**, Logarithm of odds (LOD) plot for geometric mean CQ IC_{50} values. The red line indicates the 95% probability threshold. **c**, Overlay of monodesethyl-chloroquine (md-CQ) and CQ LOD plots. A/M, apicoplast/mitochondria (these are always coinherited). The highest LOD peaks for CQ and md-CQ align with *pfcrt* on chromosome 7 and the segment including *ftsh1* on chromosome 12. Note that *dmt1* was not within the dominant chromosome 7 peak for CQ or md-CQ, unlike for quinine.

Extended Data 6

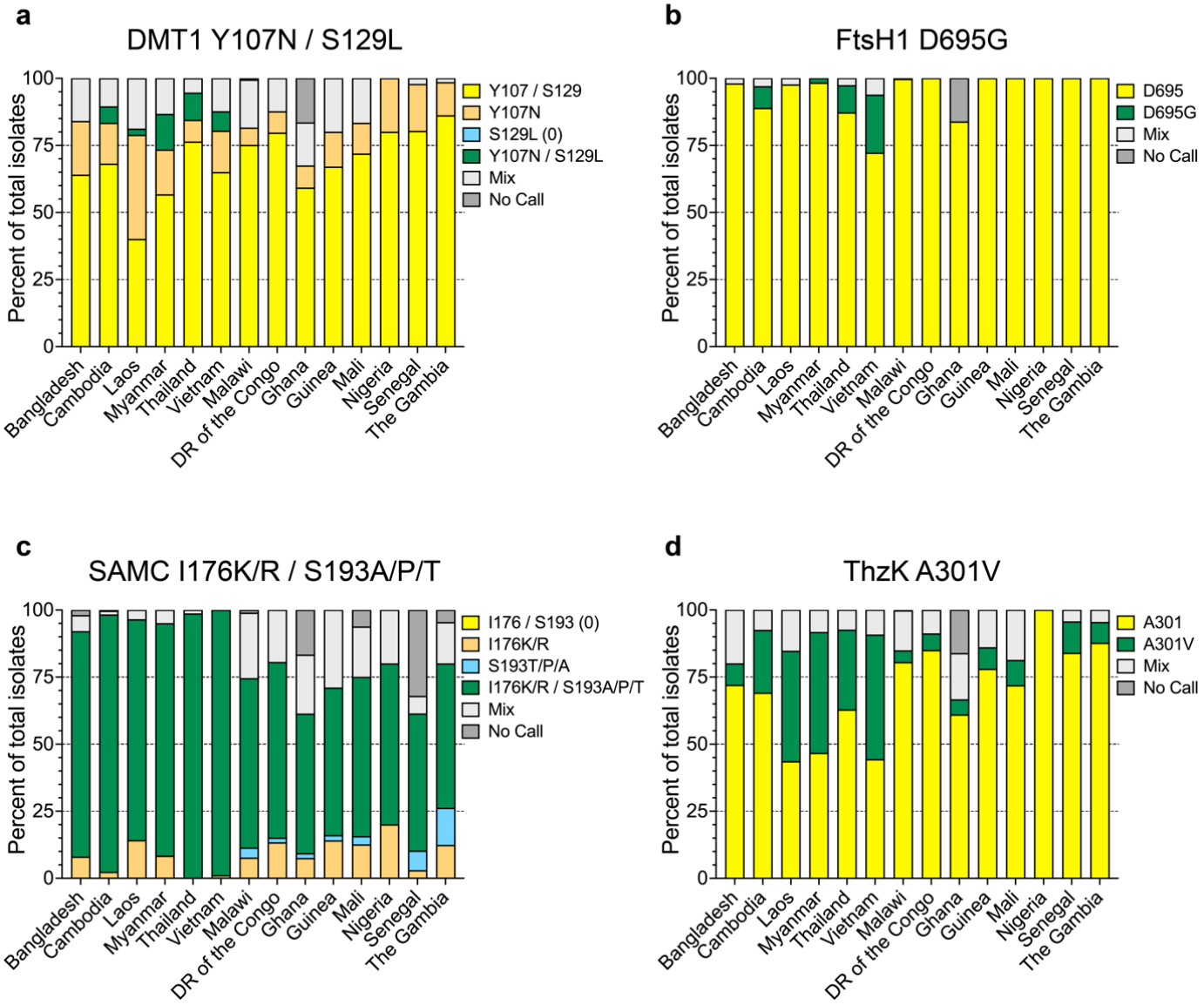

Extended Data 6 | Clinical isolates harbor mutations in genes of interest within the chromosome 7 QN and chromosome 12 quinine (QN), chloroquine (CQ), and monodesethyl-CQ (md-CQ) quantitative trait locus segments.
a-d, Frequency of the Cam3.II mutations in clinical isolates (Pf3k) of genes in chromosome 7 ((**a**), *dmt1:* PF3D7_0715800) and chromosome 12 ((**b**) *ftsh1:* PF3D7_1239700, (**c**) *samc:* PF3D7_1241600, (**d**) *thzk:* PF3D7_1239600)) loci, grouped by sampling country. Yellow indicates isolates with the NF54 wild-type haplotype covered by the indicated SNP positions; green, the Cam3.II mutant haplotype; light grey, mixed call; dark grey, genotype not called; orange or blue, single-amino acid mutants not corresponding to the double-mutant Cam3.II haplotype. (N=50 (Bangladesh), 570 (Cambodia), 85 (Laos), 60 (Myanmar), 148 (Thailand), 97 (Vietnam), 369 (Malawi), 113 (Democratic Republic of the Congo), 617 (Ghana), 100 (Guinea), 96 (Mali), 5 (Nigeria), 137 (Senegal), 65 (The Gambia); total=2,512 samples). These four top candidate genes are further described in **Fig. 3a**.

Extended Data 7

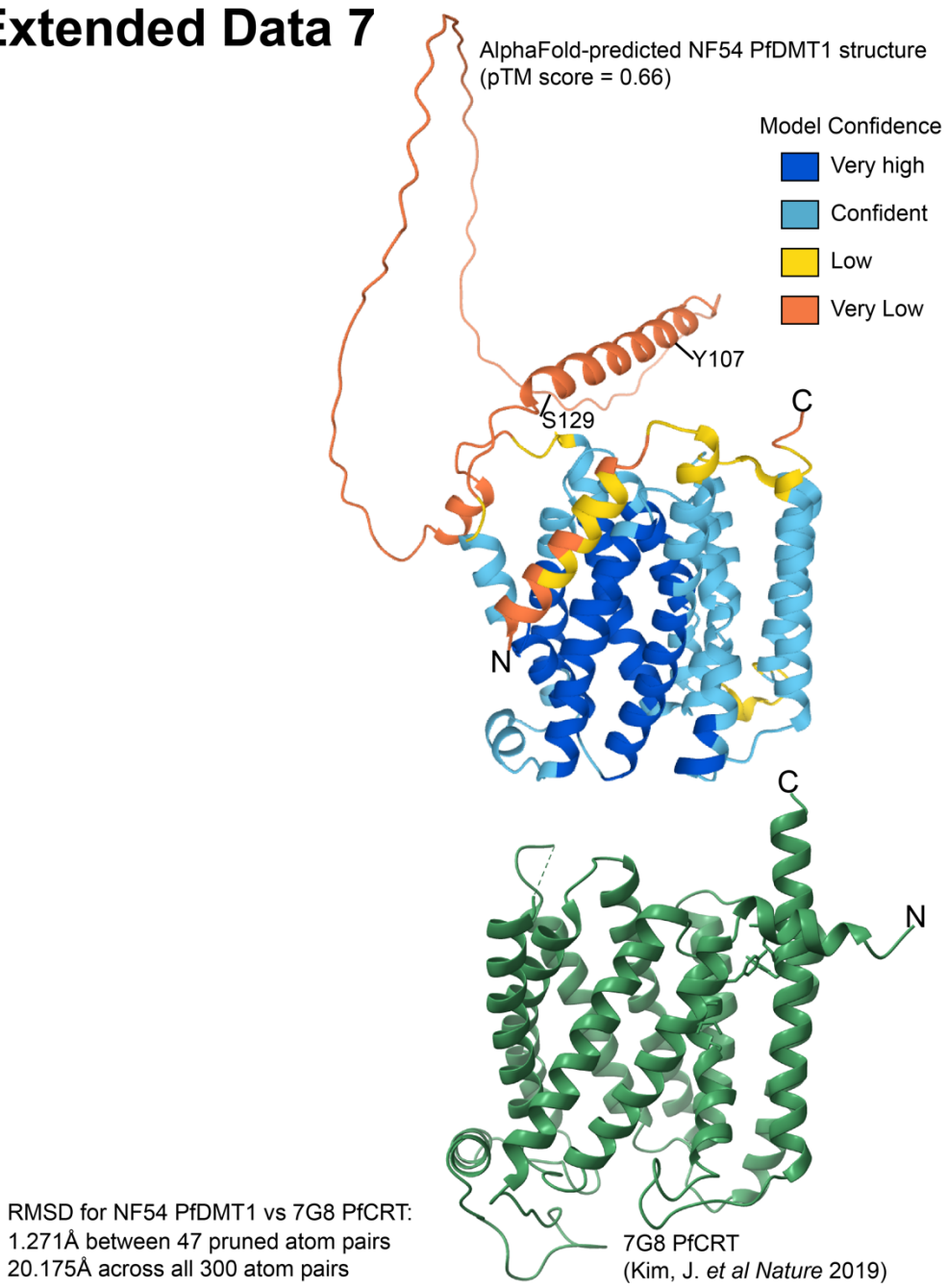

Extended Data 7 | PfDMT1 is structurally similar to another drug metabolite transporter superfamily protein, PfCRT.
Side-by-side comparison of the AlphaFold-predicted NF54 DMT1 structure and the cryo-EM-derived 7G8 PfCRT structure[47]. The predicted template modeling (pTM) is indicated for the AlphaFold NF54 DMT1 structure, which exceeds the 0.5 threshold for predicted fold reliability. The Y107 and S129 positions are indicated on the AlphaFold DMT1 structure. Root mean square deviation (RMSD) scores calculated in ChimeraX MatchMaker are indicated for PfCRT and DMT1.

Extended Data 8

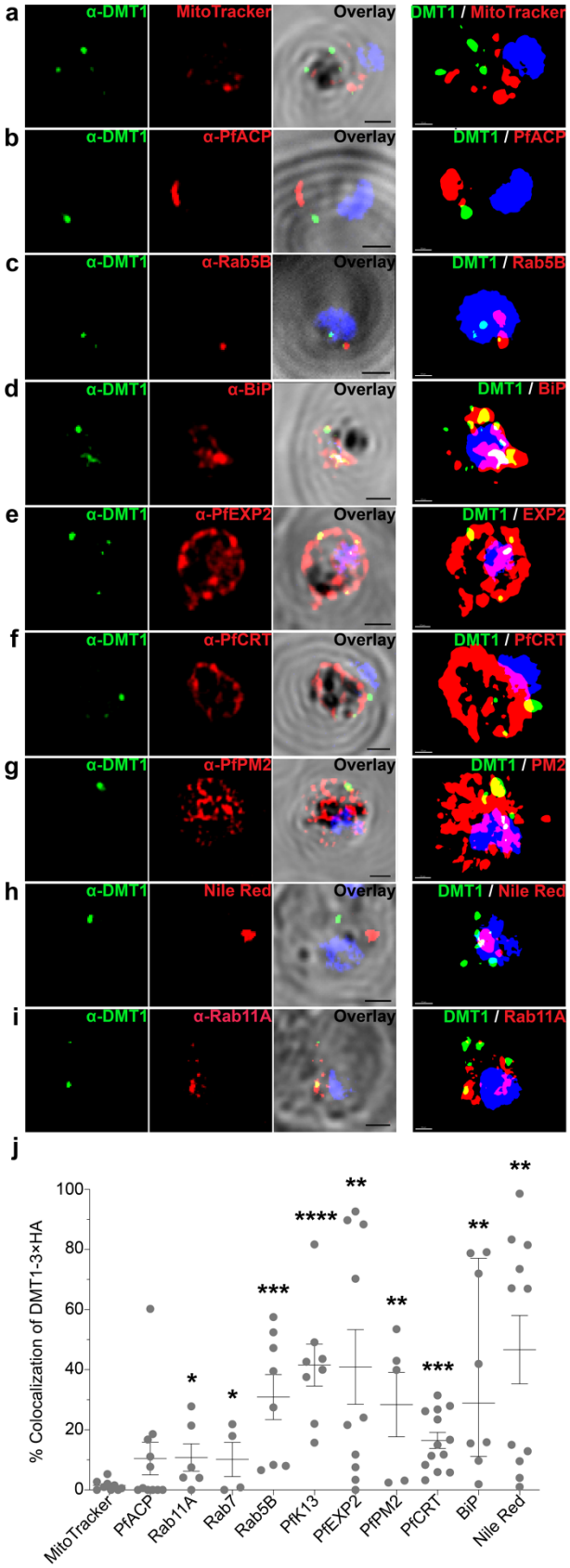

Extended Data 8 | DMT1 shows localization to structures associated with vesicular trafficking as well as the digestive vacuole.

a-i, Representative immunofluorescence assays (IFA) showing DMT1-3×HA-tagged parasites stained with α-HA (DMT1, green) and DAPI (nuclear, blue), as well as antibodies or dyes: (**a**) MitoTracker Red CMXRos (mitochondria, red), (**b**) α-PfACP (apicoplast), (**c**) α-Rab5B (early endosome), (**d**) α-BiP (ER), (**e**) α-PfEXP2 (parasitophorous vacuolar membrane), (**f**) α-PfCRT (digestive vacuole membrane), (**g**) α-PfPM2 (digestive vacuole), (**h**) Nile Red (lipid bodies), or (**i**) α-Rab11A (post-Golgi). IFA images are also shown as 3D volume reconstructions (right-most column). Scale bars: 1 μm for IFA (black) or 0.5 μm for 3D volume reconstructions (white). **j**, Mean ± SEM percent DMT1-3×HA colocalization between DMT1 and the aforementioned organelles. Colocalization *p*-values (Student's *t*-test): $^{*}p < 0.05$; $^{**}p < 0.01$; $^{***}p < 0.001$; $^{****}p < 0.0001$. Numbers of individual parasites analyzed and mean ± SEM and *p*-values for two different colocalization metrics (volume and Manders' coefficient) are described in **Table S11**.